

The Pennsylvania State University

The Graduate School

College of Engineering

**FREE-SPACE OPTICAL COMMUNICATIONS THROUGH THE SCATTERING
MEDIUM: ANALYSIS OF SIGNAL CHARACTERISTICS**

A Thesis in

Electrical Engineering

by

Binbin Wu

© 2007 Binbin Wu

Submitted in Partial Fulfillment
of the Requirements
for the Degree of

Doctor of Philosophy

December 2007

The thesis of Binbin Wu was reviewed and approved* by the following:

Mohsen Kavehrad
Professor of Electrical Engineering
Thesis Adviser
Chair of Committee

Ruyan Guo
Professor of Electrical Engineering

Shizhuo Yin
Professor of Electrical Engineering

Nadine Barrie Smith
Associate Professor of Bioengineering Engineering

W. Kenneth Jenkins
Professor of Electrical Engineering
Head of the Department of Electrical Engineering

*Signatures are on file in the Graduate School.

ABSTRACT

Free-space optical communications (FSOC) is a method by which one transmits a modulated beam of visible or infrared light through the atmosphere for broadband applications. Fundamental limitations of FSOC arise from the environment through which light propagates. This thesis addresses transmitted light signal dispersion (spatial and angular dispersion) and attenuation in FSOC operating in the scattering medium. Light signals transmitted through the scattering medium will interact with particles along the propagation path. Attenuation of light signals propagating through the medium is a combined effect of dispersion (spatial and angular) and absorption by particles. This thesis shows that the physical properties of the scattering medium play important roles in determining signal attenuation and dispersion of received light signals. A model based on ray tracing is developed to investigate light propagating through the medium. A computer simulation model of ray tracing is presented, as well.

This thesis investigates the correlation between spatial and angular dispersion of received light signals, which has significant effects on receiver design. Moreover, this thesis points out that scattering loss (loss caused by aerosol scattering) strongly depends on the receiver aperture size, field-of-view (FOV) and the position of the receiver relative to the optical axis of the transmitter.

Two categories of the scattering media are considered: clouds and battlefield particles. Cumulus cloud and fog oil (battlefield particles) are selected as the representatives of scattering media for the computer simulations. Since the scattering effects of cumulus cloud and fog oil particles are substantially different, different approaches of receiver designs are proposed. A fog oil type of medium requires a sensitive receiver with a small FOV so that it can find the line-of-

sight (LOS) photons and work with them, since only the LOS photons are meaningful to the FSOC system. For cumulus cloud, if a small value of optical thickness is concerned, a receiver with a small FOV is needed to find the LOS photons and work with them. However, a large value of optical thickness requires multiple receivers with a large FOV to capture the scattered energy and maintain the link availability.

This thesis develops a method of measuring the particle density of smoke. The particle density of smoke (man-made particles such as fog oil particles) is a key factor in the computer simulations. Different particle density may lead to different simulation results, which require rescaling of the simulation results. An experiment is then carried out to demonstrate the feasibility of the method.

The results in this thesis describe only specific scenarios for given types of scattering media and the physical size of the receiver. Generalization of the results requires additional work.

TABLE OF CONTENTS

	Page
LIST OF TABLES.....	viii
LIST OF FIGURES.....	ix
ACKNOWLEDGEMENTS.....	xii
 Chapter 1 Introduction.....	 1
1.1 Motivation.....	1
1.2 Objective.....	4
1.3 Review previous research.....	8
1.4 Research interest of the thesis.....	9
1.5 Outline.....	10
1.6 Organization.....	11
 Chapter 2 Physical properties of the scattering media.....	 13
2.1 Introduction.....	13
2.2 A single photon-particle interaction.....	14
2.3 Properties of scattering coefficients and phase functions for clouds and battlefield particles.....	 16
2.3.1 Particle size distribution of the battlefield particles.....	18
2.3.2 Particle size distribution of cumulus cloud.....	21
2.3.3 Properties of cumulus cloud and battlefield particles at wavelength $1.55\mu m$	21
2.4 Particle density of smoke.....	25

2.5 Conclusions.....	28
Chapter 3 Model of ray tracing.....	29
3.1 Introduction.....	29
3.2 Photons traveling through the 3-D space.....	30
3.3 Axis rotation.....	31
3.3.1 Parameter definitions.....	33
3.3.2 System description.....	34
3.3.3 Rotation transformation.....	35
3.4 Conclusions.....	38
Chapter 4 Monte Carlo Ray Tracing (MCRT).....	39
4.1 Introduction.....	39
4.2 Model of computer simulations of ray tracing.....	40
4.3 Parameters of the receiver.....	43
4.4 Conclusions.....	44
Chapter 5 Computer simulation results and analysis.....	47
5.1 Introduction.....	47
5.2 Relation between energy loss and FOV without pointing error ($BC = 0$).....	48
5.3 Property of spatial and angular dispersion of the received photons distributed in the receiver plane ($z_1 = Lch$).....	52
5.4 Property of the photon density distribution in the $x - y$ receiver plane.....	61

5.5 Receiver design for the two media.....	67
5.6 Analysis of computer simulation results for the two media.....	71
5.7 Conclusions.....	76
Chapter 6 Experimental results for cigarette smoke.....	78
6.1 Introduction.....	78
6.2 Reasons for selecting cigarette smoke in the experiment.....	79
6.3 Experimental setup.....	81
6.4 Experimental procedure and results.....	81
6.5 Particle density of cigarette smoke for the four-cigarette case.....	84
6.6 Monte Carlo computer simulation results of cigarette smoke.....	85
6.7 Conclusions.....	87
Chapter 7 Conclusions and future work.....	89
7.1 Conclusions.....	89
7.2 Scattering effects of the fog oil particles and receiver design issues.....	90
7.3 Scattering effects of the cumulus cloud II particles and receiver design issues.....	91
7.4 Future work.....	93
Bibliography.....	94

LIST OF TABLES

	Page
Table-1. The parameters of Equation 2.13 and the refractive index at wavelength $1.55\text{ }\mu\text{m}$ for the single modal particles.....	19
Table-2. The parameters of Equation 2.13 and the refractive index at wavelength $1.55\text{ }\mu\text{m}$ for the bi-modal particles.....	20
Table-3. The parameters of Equation 2.13 and the refractive index at wavelength $1.55\text{ }\mu\text{m}$ for the tri-modal particles.....	20
Table-4. Parameters of Equation 2.14 for cumulus cloud.....	21
Table-5. Physical properties of particles at wavelength $1.55\text{ }\mu\text{m}$	22
Table-6. Mean of scattering angle θ , P_{abs} and D_{ave} for particles at wavelength $1.55\text{ }\mu\text{m}$	25
Table-7. Experimental results of light transmitted through the smoke chamber.....	83
Table-8. Normalized scattering coefficient $k_{normsca}$ at the visible wavelength for particle size $0.143\text{ }\mu\text{m}$	84
Table-9. Particle density of cigarette smoke.....	85
Table-10. Summarization of the parameters used for the Monte Carlo computer simulation.....	85

LIST OF FIGURES

	Page
Figure 1. An example of FSOC operating in the ground-to-air, air-to-air and air-to-ground link.....	5
Figure 2. Smoke generated by smoke generators.....	5
Figure 3. A geometrical description of Equation 1.1.....	6
Figure 4. A photon encounters a particle (a single scattering event).....	15
Figure 5. Phase functions (PDFs) of cumulus cloud and battlefield particles at wavelength $1.55\mu m$ in logarithmic scales.....	24
Figure 6. A geometrical description of Equation 2.21.....	26
Figure 7. Description of the general rotation algorithm.....	32
Figure 8. A computer simulation scheme of ray tracing.....	41
Figure 9. Energy loss versus FOV half-angle. Optical thickness $\tau = 1$ and aperture size is $10cm$ in radius.....	49
Figure 10. Energy loss versus FOV half-angle. Optical thickness $\tau = 5$ and aperture size is $10cm$ in radius.....	49
Figure 11. Energy loss versus FOV half-angle. Optical thickness $\tau = 9$ and aperture size is $10cm$ in radius.....	50
Figure 12. Energy loss versus FOV half-angle. Optical thickness $\tau = 13$ and aperture size is $10cm$ in radius.....	50
Figure 13. Energy loss versus FOV half-angle. Optical thickness $\tau = 17$ and aperture size is $10cm$ in radius.....	51
Figure 14. Scheme of the 2-D histogram of spatial and angular dispersion.....	53

Figure 15. A ring with radius r in the $z_1 = Lch$ receiver plane.....	53
Figure 16. 2-D histogram of spatial and angular dispersion of the received photons distributed in the receiver plane. $\tau = 1$	55
Figure 17. 2-D histogram of spatial and angular dispersion of the received photons distributed in the receiver plane. $\tau = 5$	56
Figure 18. 2-D histogram of spatial and angular dispersion of the received photons distributed in the receiver plane. $\tau = 9$	57
Figure 19. 2-D histogram of spatial and angular dispersion of the received photons distributed in the receiver plane. $\tau = 13$	58
Figure 20. 2-D histogram of spatial and angular dispersion of the received photons distributed in the receiver plane. $\tau = 17$	59
Figure 21. Photon density distribution in the $x - y$ receiver plane. $\tau = 1$	62
Figure 22. Photon density distribution in the $x - y$ receiver plane. $\tau = 5$	63
Figure 23. Photon density distribution in the $x - y$ receiver plane. $\tau = 9$	64
Figure 24. Photon density distribution in the $x - y$ receiver plane. $\tau = 13$	65
Figure 25. Photon density distribution in the $x - y$ receiver plane. $\tau = 17$	65
Figure 26. Energy loss (E_r/E_t) versus optical thickness for different FOV half-angles and BC	69
Figure 27. Simulation scheme for generating Figure 26.....	70
Figure 28. Multiple receivers located around the LOS area of the receiver plane.....	70
Figure 29. The histogram of the number of scattering events. $\tau = 1$	72
Figure 30. The histogram of the number of scattering events. $\tau = 5$	73

Figure 31. The histogram of the number of scattering events. $\tau = 9$	74
Figure 32. The histogram of the number of scattering events. $\tau = 13$	75
Figure 33. The histogram of the number of scattering events. $\tau = 17$	75
Figure 34. An experiment for light propagating through cigarette smoke.....	79
Figure 35. Scheme of the experimental setup.....	82
Figure 36. The phase function of cigarette smoke in logarithmic scales at the visible wavelength.....	86
Figure 37. Energy loss versus FOV half-angle for the four-cigarette case.....	86

ACKNOWLEDGEMENTS

I would like to express my sincere gratitude to my principal advisor, Dr Mohsen Kavehrad, for his helpful discussions and support throughout the course of this work. I would also like to acknowledge my supervisory committee members, Dr. Ruyan Guo, Dr. Shizhuo Yin and Dr. Nadine Barrie Smith, for their valuable suggestions and comments.

I would like to thank my wife, Chunlian Yang, for proofreading this thesis. Her instruction in writing style and grammar of this thesis has been of great value. Without her support, this thesis could not have been written.

Chapter 1

Introduction

1.1 Motivation

Due to the ever-increasing demand for bandwidth, and the demonstrated success of wireless optical communications in providing broadband communications, interest in further expanding the deployment of wireless optical transmission for military communications has grown. While radio frequency (RF) communications still dominates military communications networks, it has been unable to meet the increasing demand for the large data rate due to two major reasons [1]: increased capacity requirements placed on commercial networks and the fact that RF spectrum is heavily regulated.

Lasers used in free-space optical communications (FSOC) operate in optical bands (terahertz portion of the spectrum) that are not regulated. Thus, FSOC provides a promising solution to support the high data rate. Moreover, the tight spatial confinement of a FSOC laser beam provides significant degrees of robustness and covertness, which play important roles in military communications. The small beam divergence of lasers minimizes interference, subsequently making the communications links difficult to intercept and tap.

However, FSOC poses several technical challenges:

- Aerosol scattering effects: small particles of the scattering medium along the propagation path of FSOC will impose spatial, angular and temporal dispersion on transmitted light signals. Particles also absorb some of the energy. Attenuation of

transmitted light signals through the propagation medium is a combined effect of dispersion (spatial and angular) and absorption by particles. Temporal dispersion (multiple-path effects) causes pulse spread limiting the data rate.

- Signal fading: signal fading tends to occur due to atmospheric turbulence, which causes fluctuations in both intensity and phase of received light signals [2]. The refractive index of the medium along the propagation path varies due to inhomogeneities in temperature and pressure of the atmosphere. Such variation causes performance degradation, and leads to an increase in the link error probability.

Understanding of the physical properties of the scattering medium on transmitted light signals is very important to the FSOC system design. The main challenges in designing a reliable communications system come from signal aberrations induced by the scattering medium. The design of a FSOC system is a complex process requiring compromises between many factors to achieve the best performance at an acceptable cost. Two important factors influence the FSOC system design: link budget and channel bandwidth.

The main purpose of the link budget is to verify that communications systems will operate as planned—that is, the message quality (error performance) will meet the specifications. The link budget monitors the gains and losses of the transmitted signal, from its inception at the transmitter until it is ultimately received at the receiver. The compilation yields how much safety margin (link margin) exists beyond what is required. As mentioned before, when light signals transmit through the scattering medium, attenuation happens due to aerosol scattering effects. Such kinds of attenuation are called scattering loss (loss caused by aerosol scattering). Scattering loss strongly depends on the receiver aperture size, field-of-view (FOV) and the position of the

receiver relative to the optical axis of the transmitter. Thus, understanding of scattering loss is important to the analysis of the link budget of the FSOC system.

Channel bandwidth strongly depends on pulse spread of received light signals. Theoretically, the bandwidth of the optical channel is enormous. However, due to multiple-scattering effects, photons arrive at receiver end at different times: some photons travel along the line-of-sight (LOS) path, which is the shortest path between the transmitter and the receiver; some photons travel along longer paths due to aerosol scattering. Thus, pulse spread is a result of multiple-path effects. This phenomenon is also called temporal dispersion. If a receiver is designed only for collecting the LOS photons, pulse spread caused by multiple-path effects is zero. As a result, the bandwidth of the optical channel is enormous. However, if a receiver is designed not only for collecting the LOS photons, but also for the photons subject to at least one scattering, the bandwidth of the optical channel reduces. Such a receiver is purported to increase the received energy to meet the link budget when a large value of optical thickness is of concern. Experimental results showed that, for some specific sizes of the receiver, pulse spread of received light signals propagating through clouds is no more than $20ns$ when optical thickness of the channel is less than 18 [3, 4].

In this thesis, scattering loss of FSOC operating in the scattering medium is considered. Signal fading caused by atmospheric turbulence and pulse spread due to multiple-path effects will not be discussed.

1.2 Objective

This thesis addresses transmitted light signal dispersion (spatial and angular dispersion) and signal attenuation in FSOC operating in the two categories of scattering media. One is clouds, and the other is battlefield particles, such as smoke, dust and sand. .

It is very important to understand the scattering effects of clouds on transmitted light signals for FSOC operating in the ground-to-air (up-link), air-to-air and air-to-ground (down-link) link. See Figure 1 for a description. In this thesis, only the ground-to-air link is considered. The ground-to-air link presents a communications scenario of a fixed earth station (transmitter) to an air-plane (receiver). Typically, the air-plane is inside clouds, and the earth station is in the clear weather. In this thesis, it assumes that, in the clear weather condition, no cloud particles exist. Thus, no scatterings happen when light propagates through the clear weather.

Light signal dispersion caused by smoke, dust and sand is common in the battlefield environment [5, 6]. Smoke is usually generated by smoke generators. They produce different types of man-made particles such as fog oil, hexachloroethane (HC), and white phosphorus (WP) particles to defeat enemy reconnaissance, surveillance and target acquisition effects. See Figure 2 for a description. Dust, such as heavy loading dust, light loading dust and high explosive (HE) dust, is the by-product of munitions and ground vehicle and helicopter operations. Understanding of light signal dispersion and signal attenuation is very important to the design of a FSOC system operating in the battlefield environment.

In this thesis, channel modeling of light signals propagating through the scattering medium is presented. The main focus of the thesis is to investigate signal characteristics for a single light pulse; therefore, the average power is undefined for such a condition. The peak

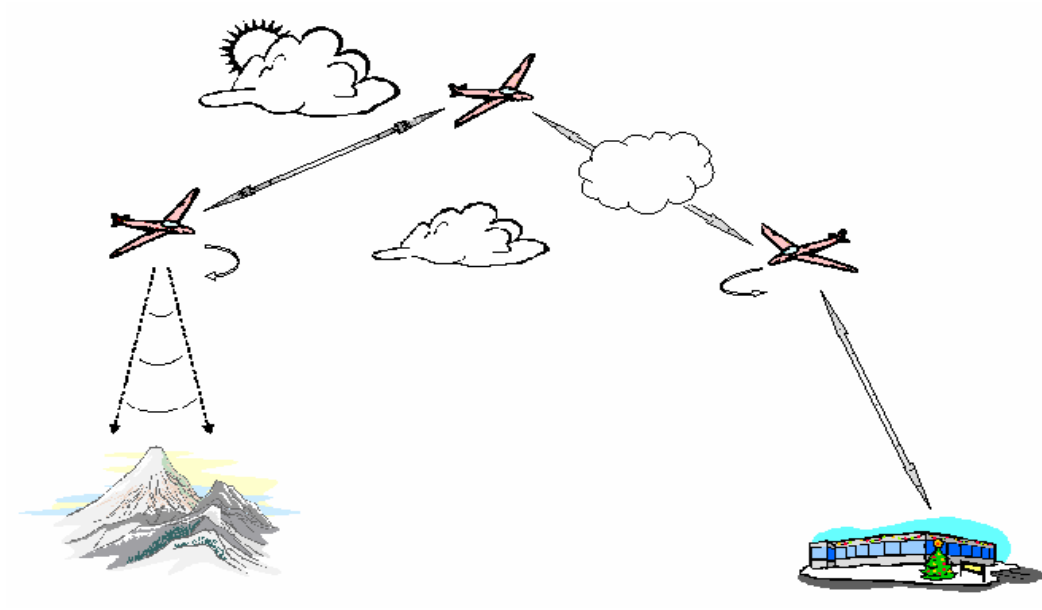


Figure 1. An example of FSOC operating in the ground-to-air, air-to-air and air-to-ground link.



Figure 2. Smoke generated by smoke generators.

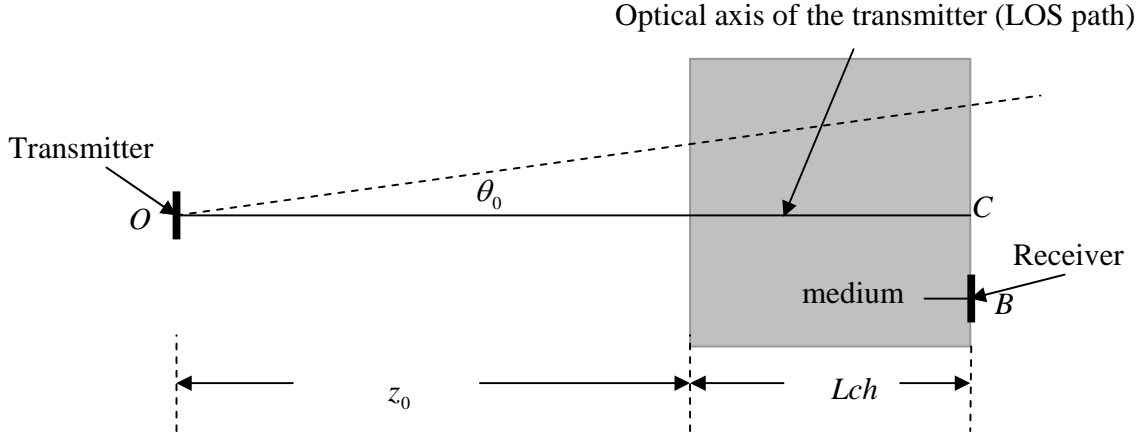


Figure 3. A geometrical description of Equation 1.1. Place a transmitter with the beam divergence half-angle θ_0 at point O . The length of the free-space (vacuum) channel is z_0 (no particles exist in the free space). The length of the scattering medium is Lch . Place a receiver with receiver area A at point B . Assume that the optical axis of the transmitter and the receiver is parallel to each other. The receiver is inside the scattering medium. The total channel length is $OC = Lch + z_0$. BC is called pointing error.

power is the primary concern in the link budget calculation. The definition of the peak power is $P = E/T$, where E represents the pulse energy in a single light pulse and T represents the time duration of a single light pulse. The link budget (path loss) equation for FSO operating in the scattering medium can be described as:

$$P_r(dB) = P_t(dB) + L_f(dB) + L_s(dB) + L_o(dB), \quad (1.1)$$

where P_r is the received peak power, P_t is the transmitted peak power, L_f is free-space loss caused by non-zero beam divergence of the light source, L_s is scattering loss caused by particles

of the scattering medium along the propagation path, and L_o is loss in transmitter and receiver optics. See Figure 3 for a description. The expression of free-space loss, L_f , is [3]

$$L_f(dB) = 10 \log_{10} \frac{A}{\pi [\theta_0 \times (z_0 + Lch)]^2}, \quad (1.2)$$

where A is the receiver area, θ_0 is the beam divergence half-angle of the light source, and $z_0 + Lch$ is the distance between the transmitter and the receiver. Parameter z_0 is the length of the free-space (vacuum) channel, and Lch is the length of the scattering medium. Calculating free-space loss L_f is straightforward. However, calculating scattering loss L_s is a challenge since it is a function of medium length Lch , medium type, the position of the receiver relative to the optical axis of the transmitter (pointing error BC) and the physical size of the receiver (aperture size and FOV). See Figure 3 for a description of pointing error BC .

None-zero values of BC are caused by pointing error. Although a high resolution tracking radar is typically used in FSOC operating in the ground-to-air link, pointing error BC can be as much as $3m$ [7]. Thus, the receiver may not be always located at point C to best receive the LOS power, and scattering loss due to pointing error has to be taken into account in the link budget calculation.

In this thesis, it assumes that the transmitter and the receiver are both inside the scattering medium, and beam divergence of the light source is zero. This is an abstraction to study the scattering effects of the medium independent of other factors. Thus, free space loss L_f and L_o are not considered. As a result, scattering loss shown in Equation 1.1 can be expressed as

$$L_s(dB) = P_r(dB) - P_t(dB) = 10 \log_{10} \left[\frac{E_r T_t}{E_t T_r} \right]$$

$$= 10 \log_{10} \left[\frac{E_r}{E_t} \right] - 10 \log_{10} \left[1 + \frac{\Delta t}{T_t} \right], \quad (1.3)$$

where E_r is the energy in a received light pulse, T_r is the time duration of a received light pulse, E_t is the energy in a transmitted light pulse, T_t is the time duration of a transmitted light pulse, and Δt is pulse spread due to scatterings, which is defined as

$$\Delta t = T_r - T_t. \quad (1.4)$$

The first term in the right side of Equation 1.3 is energy loss (E_r/E_t) caused by scatterings. The second term is loss due to pulse spread. If a receiver is designed only for collecting the LOS photons (pulse spread $\Delta t = 0$), scattering loss is the same as energy loss.

1.3 Review previous research

Aerosol scattering effect has been studied extensively, and various theoretical models have been proposed to describe it [8, 9]. These models, however, did not consider the physical size of the receiver and signal attenuation (scattering loss). Basically, it assumed that the aperture size of the receiver is infinity. In [10-12], the authors applied a ray-tracing method and assumed that the receiver could always collect 5% of the total transmitted energy from the light source regardless of the length of the channel. As a result, signal attenuation is always fixed (5%), and the physical size of the receiver is undefined.

In communications systems, only photons collected by the receiver are meaningful. In this thesis, a receiver with a finite aperture size and FOV is used to collect the received photons. In addition, pointing error BC is taken into account for calculating energy loss. As a result, energy loss is for that receiver and the specific value of BC .

1.4 Research interest of the thesis

This thesis considers energy loss (E_r/E_t) shown in Equation 1.3. Loss caused by pulse spread Δt is not considered. Energy loss (E_r/E_t) strongly depends on the physical properties of the scattering medium. Some media have strong scattering effects on the incident light; others do not. Two types of scattering media are selected for analysis in this thesis: clouds and battlefield particles. A ray-tracing model is developed to simulate light propagating through the scattering medium. It shows that light signal dispersion for the two types of scattering media is different. The correlation between spatial and angular dispersion of the received light signal is presented, which is substantially different for the two scattering media. Different receiver designs are proposed based on the properties of light signal dispersion. The relation among received energy E_r , receiver aperture size, FOV and pointing error BC is investigated, as well. Understanding this relation is very important to the link budget calculation and receiver design issues.

In the computer simulations, cumulus cloud is chosen as a representative of scattering media from various types of cloud because it is frequently found in low level altitudes [13]. It is generally located at elevations between 200 and 20,000 feet, which is very relevant for FSOC operating at the ground-to-air link. Light signal dispersion caused by fog oil particles, is common in the battlefield environment. Thus, fog oil particles are selected as the representative scattering media in the battlefield environment.

The wavelength of FSOC is selected as $1.55\mu m$, since it is commonly used in single-mode fiber, and amplification in optical domain is available at this wavelength [14, 15].

A method calculating the particle density of smoke (man-made particles such as fog oil particles) is proposed in this thesis, as well. The particle density of smoke is a key factor in the computer simulations. Different particle density may lead to different simulation results, which

requires rescaling of the simulation results. This thesis develops a method of measuring the particle density of smoke. An experiment is then carried out to demonstrate the feasibility of the method.

1.5 Outline

Reliable communications require a good understanding of the surrounding environment that affects the communications channel. The fundamental limitation of FSOC arises from the environment through which light propagates. This thesis presents the effects of the physical properties of the scattering medium upon transmitted light signals. Two types of scattering media are selected: clouds and battlefield particles. It shows that phase functions and scattering coefficients play important roles in the analysis of the scattering effects of particles.

The thesis then introduces a model of ray tracing of light signals transmitted through the scattering medium. The Monte Carlo computer simulation of the ray-tracing model is used to investigate spatial and angular dispersion of light signals. Energy loss is the direct result of spatial and angular dispersion. A receiver with a finite physical size and FOV is used in the computer simulations to collect photons.

The correlation between spatial and angular dispersion of received light signals is investigated, which has significant effects on receiver design issues. Moreover, this thesis indicates that energy loss strongly depends on the receiver aperture size, FOV and the position of the receiver relative to the optical axis of the transmitter (pointing error BC).

Cumulus cloud and fog oil are selected as representatives of clouds and battlefield particles in the computer simulations, respectively. The wavelength of FSOC is chosen as $1.55\mu m$.

Based on simulation results, receiver designs are proposed for the two scattering media. For the fog oil type of the medium, a sensitive receiver with a small FOV is needed that can find the LOS photons and work with them. For cumulus cloud, if a small value of optical thickness is of concern in FSOC, a sensitive receiver with a small FOV is needed that can find the LOS photons and work with them. However, if a large value of optical thickness is of concern, multiple receivers with a large FOV located around the LOS area may need to capture the scattered photons and maintain the link availability.

A method calculating the particle density of smoke is developed. Cigarette smoke is selected in the experiment to demonstrate the feasibility of the method. Moreover, the computer simulations of cigarette smoke are presented. The simulation results match the experimental results. It shows that the ray-tracing model is a good model simulating light transmitted through smoke.

The results in this thesis describe only specific scenarios for given types of scattering media and the physical size of the receiver. Generalization of the results requires additional work.

1.6 Organization

This thesis is organized as follows: physical properties of clouds and battlefield particles are discussed in Chapter 2. A method calculating the particle density of smoke is presented in this chapter, as well. Chapter 3 introduces a model of ray tracing simulating light signals transmitted through the scattering medium. Chapter 4 presents the Monte Carlo computer simulation of the ray-tracing model. Simulation results and analysis of spatial and angular dispersion of received light signals are discussed in Chapter 5. In this chapter, the relation among energy loss (E_r/E_t), physical size of the receiver (aperture size and FOV) and the position of the

receiver relative to the optical axis of the transmitter (pointing error BC) is investigated, as well. Moreover, in the same chapter, receiver designs are proposed for the two scattering media. Experimental results for light transmitted through cigarette smoke are presented in Chapter 6. In this chapter, the particle density of cigarette smoke is calculated based on the method developed in Chapter 2. Chapter 7 completes this thesis with conclusions.

Chapter 2

Physical properties of the scattering media

2.1 Introduction

In order to understand the surrounding environment that affects the communications channel, it is essential to understand the physical properties of the scattering medium. As mentioned in Chapter 1, light signals transmitted through the scattering medium will interact with particles along the propagation path. A light pulse consists of numerous photons. Thus, the effects of the medium (particles) on the transmitted light (photons) can be treated as a photon-particle interaction. The particles can be man-made particles generated by smoke generators, such as fog oil particles. They also can be water droplets, such as cloud particles.

The photon-particle interaction depends on the size distribution of particles, the particle density and the refractive index of the scattering medium at a specific wavelength. For some types of the scattering medium, such as smoke, the photon-particle interaction is so strong that the medium scatters most of the energy of transmitted light signals. Two physical properties of particles determine the photon-particle interaction: scattering phase functions and coefficients. The following discussion will analyze the physical properties of clouds and battlefield particles.

Moreover, an analytic formula is developed to calculate the particle density of smoke. Smoke is the man-made particles and the particle density of smoke strongly depends on the method of smoke generations. The scattering coefficient of particles is a linear function of the particle density, and plays an important role in the computer simulation results. In order to

accurately calculate the scattering coefficient of the smoke particles, the particle density has to be known first.

This chapter is organized as follows: a single photon-particle interaction is introduced in Section 2.2. Section 2.3 introduces several assumptions necessary for calculating phase functions and scattering coefficients. The particle size distribution and the particle density for clouds and battlefield particles are shown in this section, as well. Section 2.4 develops an analytic formula for calculating the particle density of smoke. Conclusions are presented in Section 2.5.

2.2 A single photon-particle interaction

Typically, the propagation of the electro-magnetic energy through the scattering medium depends on the wavelength of the light signal and the type of the medium being traversed. The medium consists of particles of various sizes suspended in the air. A light pulse transmitted through the medium consists of numerous photons. Thus, the effect of the medium on transmitted light singles can be treated as a photon-particle interaction: when a photon encounters a particle, it is either absorbed by the particle with a probability P_{abs} or scattered away with a scattering angle θ . Figure 4 depicts the photon-particle interaction for a single scattering event.

The probability of absorption in a single scattering event is given by [16]

$$P_{abs} = 1 - \omega, \quad (2.1)$$

where parameter ω is the probability that interacting radiation is scattered rather than absorbed, and is called the single-scatter albedo. Parameter ω is defined as

$$\omega = \frac{k_s}{k_e} = \frac{k_s}{k_s + k_a}. \quad (2.2)$$

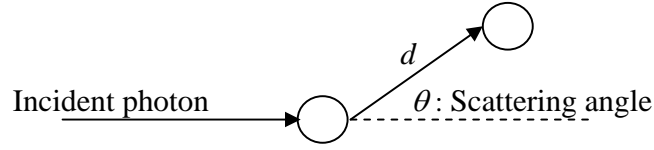


Figure 4. A photon encounters a particle (a single scattering event). The photon is either absorbed by the particle with a probability P_{abs} or scattered away with a scattering angle θ . Variable d is the traveling distance between two consecutive scatterings.

In Equation 2.2, which deals with the energy of the light source (proportional to the number of the photons affected), k_e is the extinction coefficient that describes the proportional energy removed from the light due to incidence on a particle, k_s is the scattering coefficient that describes the radiation energy scattered out due to incidence on a particle and k_a is the absorption coefficient that describes the amount of the energy absorbed by a particle. Taking Equation 2.2 to Equation 2.1, one obtains

$$P_{abs} = \frac{k_a}{k_e}. \quad (2.3)$$

Thus, the probability of absorption P_{abs} is the ratio of k_a to k_e .

Scattering angle θ shown in Figure 4 is treated as a random variable, and it is defined as the angle between the direction of the incident path and that of the scattering path. In Mie theory, the probability distribution function (PDF) of scattering angle θ is called the phase function. The details of the phase function will be discussed in Section 2.3.

The PDF of random variable d shown in Figure 4 is assumed to be an exponential [10, 11, 12, 17, 18]:

$$p(d) = (1/D_{ave}) \exp(-d/D_{ave}), \quad (2.4)$$

where D_{ave} is the mean of d . The expression of parameter D_{ave} is

$$D_{ave} = \frac{1}{k_s}. \quad (2.5)$$

For non-absorption medium, $k_s \approx k_e$. Thus, the value of D_{ave} can be approximately as $(1/k_e)$.

According to Mie theory [16, 17, 18, 19], absorption probability P_{abs} , scattering coefficient k_s (D_{ave}), extinction coefficient k_e and the PDF of scattering angle θ are decided by the particle size distribution, the particle density and the refractive index of particles at a specific wavelength, which will be discussed in Section 2.3.

Absorption probability P_{abs} and the PDF of scattering angle θ provide enough information to predict a single scattering event. However, when photons travel through the scattering medium, multiple scatterings may happen before photons reach the medium edge. Further discussion on multiple scatterings is presented in Chapter 3.

2.3. Properties of scattering coefficients and phase functions for clouds and battlefield particles

The photon-particle interaction for a single scattering event can be fully understood through Maxwell's equations. Mie theory is a complete analytical solution of Maxwell's equations for the scattering of the electromagnetic energy by dielectric spherical particles. According to Mie theory, the probability of absorption P_{abs} (k_s and k_e), the PDF of random variable θ and the value of D_{ave} are calculated based on the particle size distribution, the particle density and the refractive index of the medium at a specific wavelength. Several assumptions are made in order to use Mie theory [16]:

- Far field conditions are satisfied. This means that the transmission distance of photons is much larger than the size of particles.
- The shape of the particle can be approximated as a sphere.
- The scattering properties of a given type of the particle distribution can be approximated as a weighted integral over the particle size distribution.

The extinction and scattering coefficients for a single radius r are defined as [17]:

$$C_e(r) = \frac{4\pi}{k^2} \text{Re}\{S_i(0, r)\} = C_a(r) + C_s(r) \text{ with } S_1(0, r) = S_2(0, r), \quad (2.6)$$

and

$$C_s(r) = \frac{1}{k^2} \int_{4\pi} S_{11}(\theta, r) d\omega. \quad (2.7)$$

where S_1 and S_2 represent the solution of the scattered electrical field in perpendicular and parallel to the scatter plane (the plane in which θ is measured). Parameters S_1 and S_2 are functions of radius r and scattering angle θ . Parameter k is the phase constant of the medium. $S_{11}(\theta, r)$ shown in Equation 2.7 is defined as

$$S_{11}(\theta, r) = 0.5 \times [|S_2(\theta, r)|^2 + |S_1(\theta, r)|^2], \quad (2.8)$$

which takes the average effects of polarizations into account. The corresponding generalization of $S_{11}(\theta, r)$ is

$$S_{11}(\theta) = \int_0^\infty S_{11}(\theta, r) n(r) dr, \quad (2.9)$$

where $n(r)$ is the particle size distribution of the medium. The integration in Equation 2.7 is over the entire solid angle. To this end, coefficients k_e , k_s and k_a can be approximated as a weighted integral over the particle size distribution:

$$k_e = \int_0^\infty C_e(r)n(r)dr = k_s + k_a , \quad (2.10)$$

and

$$k_s = \int_0^\infty C_s(r)n(r)dr . \quad (2.11)$$

For a polydispersion, the phase function is defined as

$$P(\theta) = \frac{4\pi.S_{11}(\theta)}{k^2.k_s} . \quad (2.12)$$

Since $S_{11}(\theta)$ takes the average effects of polarizations into account, phase function $P(\theta)$ represents the un-polarized light.

2.3.1 Particle size distribution of the battlefield particles

The particle size distribution of the battlefield particles is treated as a log-normal distribution as follows [16, 20]:

$$n(r) = \sum_{i=1}^m \frac{N_0}{\sqrt{2\pi r \ln \sigma_g}} \exp\left[-\frac{1}{2}\left(\frac{\ln r - \ln r_{gn}}{\ln \sigma_g}\right)^2\right], \quad (2.13)$$

where parameter m is the number of modes that density function $n(r)$ has, variable r is the radius of particles in μm unit, N_0 is the total number of particles per volume of air in cc^{-1} unit, r_{gn} is the geometric mean radius in μm unit and σ_g is the geometric mean standard deviation.

The particle size distributions of fog oil, hexachloroethane (HC), and white phosphorus (WP) particles are single mode distributions ($m=1$). Table-1 illustrates the parameters of Equation 2.13 and the refractive index at wavelength $1.55\mu m$ for these types of particles. The densities of fog oil and HC particles are taken from the work of Farmer, Morris and Schwartz

Table-1. The parameters of Equation 2.13 and the refractive index at wavelength $1.55 \mu m$ for the single modal particles.

Medium types	$N_0 (cc^{-1})$	$r_{gn} (\mu m)$	σ_g	Refractive index at wavelength $1.55 \mu m$
Fog oil	1.07×10^6	0.142	1.8	$1.4735 + 1.05 \times 10^{-5} j$
HC at Hum ^a 85%	0.576×10^6	0.42	1.45	$1.68 + 1.05 \times 10^{-5} j^b$
WP at Hum 17%	1	0.24	1.45	$1.4205 + 0.415 \times 10^{-2} j$
WP at Hum 50%	1	0.27	1.45	$1.391 + 0.299 \times 10^{-2} j$
WP at Hum 90%	1	0.37	1.45	$1.341 + 0.0988 \times 10^{-2} j$

^a : Humidity.

^b : Refractive index of HC particles at the visible wavelength.

[21]. The refractive index of HC particles at wavelength $1.55 \mu m$ is not found in the literature, so the refractive index of HC particles at the visible wavelength is used [22]. Particle densities N_0 of WP particles will vary greatly, depending on the method of smoke productions, so the value of N_0 for WP particles is left as $1 cc^{-1}$.

The particle size distributions of light loading dust and high explosive dust (HE) are bi-modal ($m = 2$). Table-2 illustrates the parameters of Equation 2.13 and the refractive index at wavelength $1.55 \mu m$ for these particles. The refractive index of HE particles at wavelength $1.55 \mu m$ is taken from the work of Ivlev and Popova [23]. Assume that the accumulation mode of the light loading dust consists of 80% of ammonium sulfate and 20% of carbon by mass (the mass of quartz is negligible). Then, the complex refractive index of the light loading dust can be deduced [24].

The particle size distribution of heavy loading dust is tri-modal ($m = 3$). Table-3 illustrates the parameters of Equation 2.13 and the refractive index at wavelength $1.55 \mu m$ for the particles. Assume that the accumulation mode of heavy loading dust consists of 80% of quartz

Table-2. The parameters of Equation 2.13 and the refractive index at wavelength $1.55 \mu m$ for the bi-modal particles.

Medium types	Light loading dust		HE dust	
Mode	Small	Large	Small	Large
Composition	Ammonium sulfate	Quartz		
$N_0\,(cc^{-1})$	1988	3.76	200	0.07
$r_{gn}(um)$	0.05	0.5	0.5	22.5
σ_g	2.0	2.0	2.6	1.87
Composition	Carbon			
$N_0\,(cc^{-1})$	488.5			
$r_{gn}(um)$	0.05			
σ_g	2.0			
Refractive index at 1.55 um	1.546 + 0.0921 <i>j</i>		1.6445 + 0.0073 <i>j</i>	

Table-3. The parameters of Equation 2.13 and the refractive index at wavelength $1.55 \mu m$ for the tri-modal particles.

Medium types	Heavy loading dust	
Mode	Small	Large
Composition	Montmorillonite	Quartz
$N_0(cc^{-1})$	39.62	0.1128
$r_{gn}(um)$	0.5	15
σ_g	2.25	1.6
Composition	Quartz	
$N_0(cc^{-1})$	1218.6	
$r_{gn}(um)$	0.5	
σ_g	1.6	
Refractive index at 1.55 um	$1.53+3.008\times10^{-5}j$	

Table-4. Parameters of Equation 2.14 for cumulus cloud.

Medium types	a	α	b	γ
Cumulus I [12]	2.373	6	1.5	1
Cumulus II [13]	2.604	3	0.5	1

and 20% of montmorillonite by mass, and the complex refractive index of the heavy loading dust can be determined.

2.3.2 Particle size distribution of cumulus cloud

The particle size distribution of cumulus cloud is treated as a double gamma function [13, 17, 25]:

$$n(r) = ar^\alpha \cdot \exp(-br^\gamma), \quad 0 \leq r < \infty \quad (2.14)$$

where variable r is the radius of particles in μm unit. Particle density N_0 , given by the integral over all particle radii, for this distribution, is

$$N_0 = a\gamma^{-1}b^{-(\alpha+1)/\gamma}\Gamma\left(\frac{\alpha+1}{\gamma}\right), \quad (2.15)$$

where symbol Γ represents the gamma function. Since the particle size distribution of clouds depends on locations, Table-4 shows the parameters of two types of cumulus cloud that are well documented. Cloud particles can be treated as water droplets, so the refractive index of cumulus cloud particles at wavelength $1.55\mu m$ is $1.3109 + 1.348 \times 10^{-4}j$.

2.3.3 Properties of cumulus cloud and battlefield particles at wavelength $1.55\mu m$

Coefficients k_e , k_s , k_a and phase functions for different types of scattering media are calculated based on the data shown in Table-1, 2, 3 and 4. In the calculations, the normalized

values of three coefficients $k_{normsca}$, $k_{normext}$ and $k_{normabs}$ are obtained first, assuming that the density of particles N_0 is equal to 1 cc^{-1} . Then, coefficients k_e , k_s , and k_a are obtained by equations:

$$k_e = k_{normext} \times N_0, \quad (2.16)$$

$$k_s = k_{normsca} \times N_0 \quad (2.17)$$

and

$$k_a = k_{normext} - k_{normsca}. \quad (2.18)$$

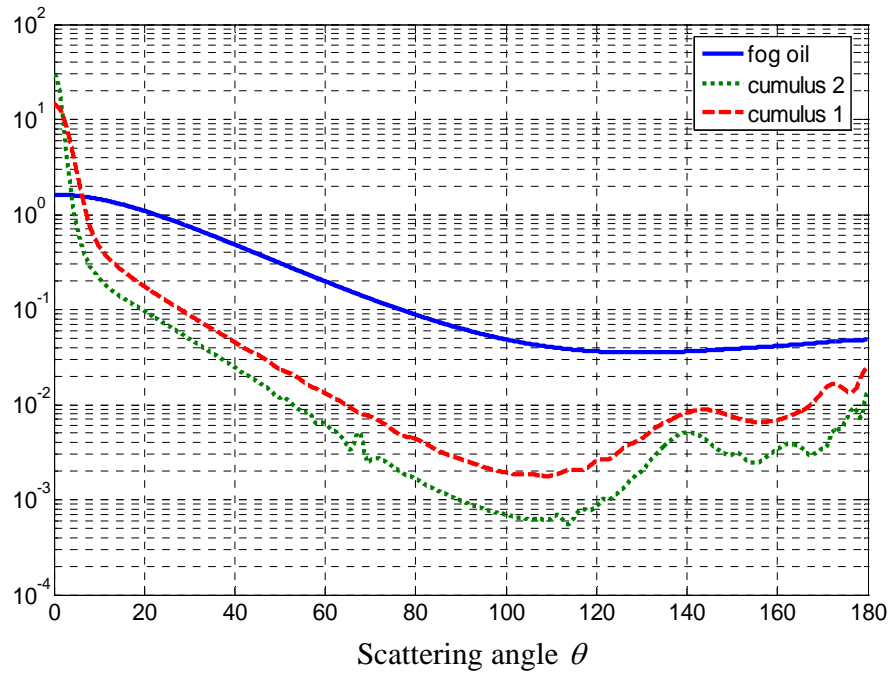
Thus, coefficients $k_{normsca}$, $k_{normext}$ and $k_{normabs}$ are independent of particle density N_0 , and are functions of the particle size distribution and the refractive index of particles at the specific wavelength. For the two types of the scattering media, the values of $k_{normsca}$ and $k_{normext}$ coefficients and their respective k_s and k_e in specific values of particle density N_0 are shown in Table-5.

Table-5. Physical properties of particles at wavelength $1.55\text{ }\mu\text{m}$.

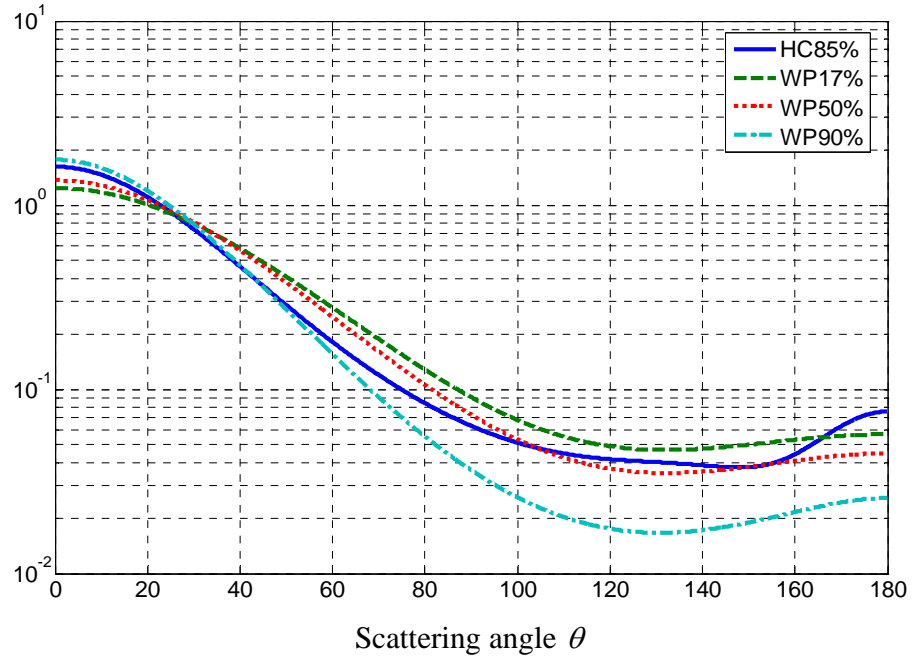
Medium type	$k_{normsca}$	$k_{normext}$	$N_0\text{ (cc}^{-1}\text{)}^a$	$k_s\text{ (km}^{-1}\text{)}$	$k_e\text{ (km}^{-1}\text{)}$
Fog oil	9.472e-5	9.473e-5	1.07e+6	101.35	101.36
HC at Hum 85%	0.002286	0.002286	5.76e+5	1316.94	1317
Light loading dust	8.724e-6	1.536e-5	2480.3	0.0216	0.0381
Heavy loading dust	0.003888	0.003889	1258.3	4.8925	4.894
HE	0.010443	0.012715	200.07	2.0892	2.5439
WP at Hum 17%	0.000126	0.0001308	1	0.00126	0.0001308
WP at Hum 50%	0.000185	0.0001902	1	0.000185	0.0001902
WP at Hum 90%	0.000542	0.0005464	1	0.000542	0.0005464
Cumulus I	0.1756	0.1767	100	17.558	17.666
Cumulus II	0.5249	0.5309	250	131.22	132.73

^a: The values of N_0 shown here are the combination density for all modes.

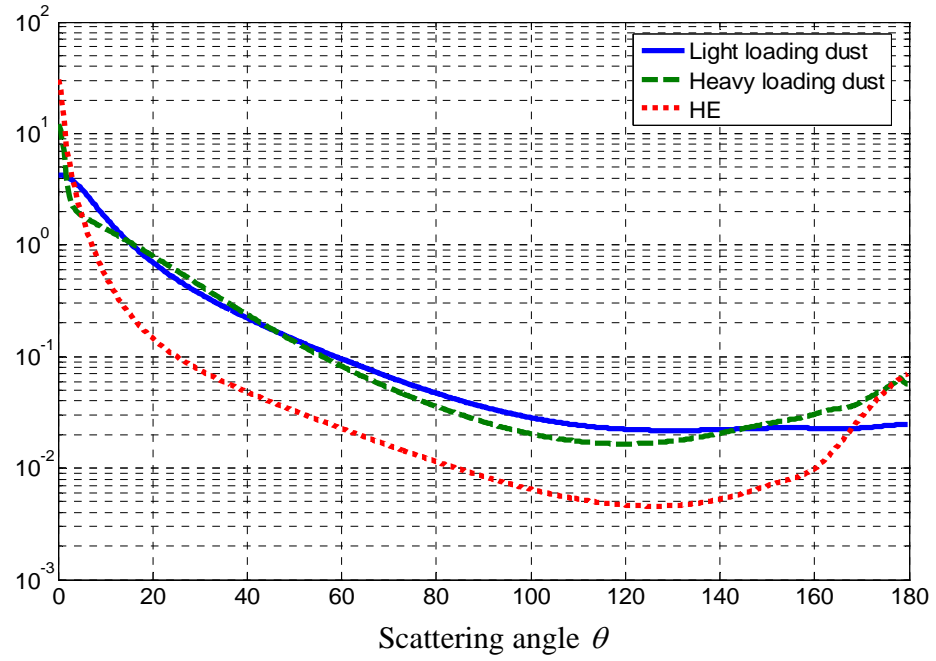
Figure 5 illustrates the phase functions of cumulus cloud and battlefield particles at wavelength $1.55\mu m$ in logarithmic scales. Figure 5 (a) shows the phase functions of cumulus cloud and fog oil particles. Figure 5 (b) shows the phase functions of HC and WP particles for different humidity. Figure 5 (c) shows the phase functions of light loading dust, heavy loading dust and HE dust. The area of the phase functions shown in these figures is normalized to one, so the phase functions can be taken as PDFs. The mean of the phase functions, D_{ave} and P_{abs} are calculated as well, shown in Table-6. Since particle density N_0 of WP particles depends on the method of smoke generations, D_{ave} of WP particles is not available.



(a). Cumulus cloud and fog oil particles.



(b). HC and WP particles.



(c). Light loading dust, heavy loading dust and HE dust

Figure 5. Phase functions (PDFs) of cumulus cloud and battlefield particles at wavelength $1.55\mu m$ in logarithmic scales.

Table-6. Mean of scattering angle θ , P_{abs} and D_{ave} for particles at wavelength $1.55\mu m$.

Medium types	$E[\theta]$	P_{abs} (%)	D_{ave} ($1/k_s$)
Cumulus I [25]	5.95°	0.61	$56.95m$
Cumulus II [13]	3.16°	1.14	$7.58m$
Fog oil	30.82°	0.0073	$9.86m$
HC at Hum 85%	31.62°	0.0046	$0.7593m$
WP at Hum 17%	36.84°	3.62	N/A
WP at Hum 50%	33.22°	2.62	N/A
WP at Hum 90%	25.37°	0.81	N/A
Light loading dust	18.74°	43.2	$46296m$
Heavy loading dust	18.87°	0.034	$204.4m$
HE	7.19°	17.9	$478.65m$

2.4 Particle density of smoke

As mentioned earlier, smoke is man-made particles and the particle density of smoke strongly depends on the method of smoke generations. Thus, the particle density of smoke may vary. Moreover, the particle density is a very important parameter for calculating scattering coefficient k_s (D_{ave}). See Equation 2.16, 2.17 and 2.18. This section shows that particle density N_0 can be calculated if un-scattered power $P_{unscattered}$ and medium length Lch are measured accurately. An analytic solution for calculating particle density N_0 is developed as follows.

A standard measure of the medium thickness along the LOS path is optical thickness τ , defined by the equation

$$\tau = Lch \times k_e. \quad (2.19)$$

If absorption effects of particles on the incident light are negligible (absorption probability P_{abs} is very small), approximation $k_e \approx k_s = (1/D_{ave})$ is valid. Thus, for cumulus cloud, fog oil, HC, WP at Hum 90% and heavy loading dust, optical thickness τ can be approximated as

$$\tau \approx Lch \times k_s = \frac{Lch}{D_{ave}}. \quad (2.20)$$

From Equation 2.20, it shows that the mean of the number of scattering events for photons transmitting through the non-absorption medium can be approximated as optical thickness τ .

Consider a light source emitting power P_t with none-zero beam divergence half-angle θ_0 . Place a receiver with receiver area A at a distance Lch from the transmitter; the length of the scattering medium is also Lch . See Figure 6 for a geometrical description. Assume that both the receiver and the transmitter are inside the medium. The power caused by the un-scattered

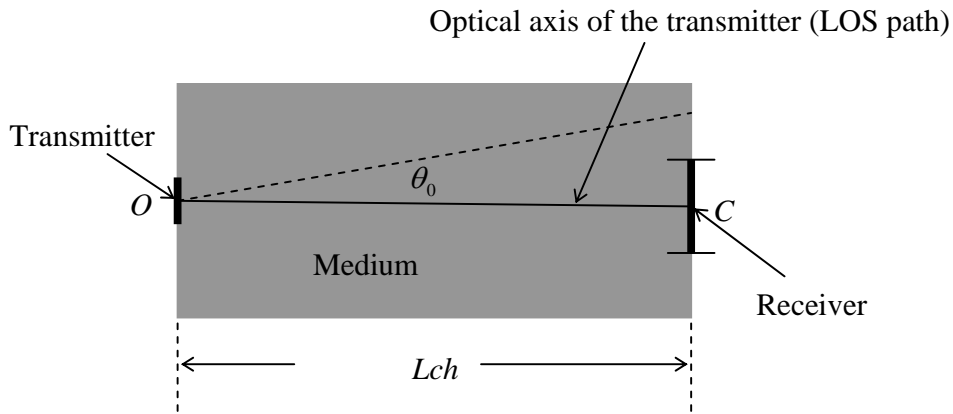


Figure 6. A geometrical description of Equation 2.21. Place a transmitter with the beam divergence half-angle θ_0 at point O . The length of the scattering medium is Lch . Place a receiver with receiver area A at point C . Both the transmitter and the receiver are inside the scattering medium.

photons is approximated as:

$$P_{unscattered} = P_t \frac{A}{\pi[\theta_0(Lch)]^2} e^{-\tau}, \quad (2.21)$$

where $P_{unscattered}$ is called the un-scattered power. The un-scattered photons are defined as the photons received by a receiver without any scatterings. The received un-scattered photons include those on the LOS path and those within sufficiently small beam half-angle such that they fall within the receiver area. The addition of the small angle photons is for the real applications with finite beam divergence from the light source. Exponential term $e^{-\tau}$ shown in Equation 2.21 accounts for LOS attenuation. Thus, Equation 2.21 not only considers free-space loss caused by non-zero beam divergence of the light source, but also LOS attenuation. The maximum area of the receiver designed to receive primarily the un-scattered photons is

$$A \leq \pi(\theta_0 \times Lch)^2. \quad (2.22)$$

For example, if a laser with beam divergence half-angle θ_0 and a receiver with the circular area are used, the radius of the receiver should be less than $\theta_0 \times Lch$. Moreover, the FOV half-angle of the receiver should be small enough to catch mostly the un-scattered photons. According to a simple geometrical rule, the FOV half-angle of the receiver should be the same order as beam divergence half-angle θ_0 of the light source.

Substituting Equation 2.17 and 2.20 into Equation 2.21, one obtains

$$N_0 = \frac{1}{Lch \times k_{normscat}} \ln\left(\frac{AP_t}{\pi(Lch \times \theta_0)^2 P_{unscattered}}\right). \quad (2.23)$$

Since coefficient $k_{normscat}$ is not a function of the particle density, Equation 2.23 offers a way to calculate particle density N_0 of the non-absorption medium if un-scattered power $P_{unscattered}$ and length of the scattering medium Lch can be measured accurately.

2.5 Conclusions

The phase functions of fog oil, HC and WP particles have no peaks in the forward-scattering direction ($\theta = 0$ direction) at all. The scattering effects of these particles on the incident photon are similar to Raleigh scattering. This means that the scattered energy is nearly uniformly distributed in all directions. Thus, even for a single scattering event, the scattering effects of smoke particle on the incident light are significant.

However, the phase functions of cumulus clouds have a very strong peak in the forward-scattering direction, especially for cumulus cloud II. The scattering effects of these cloud particles on the incident light are similar to Mie scattering: the scattered energy has a very strong peak in the forward-scattering direction. In a single scattering event, the scattering effects of cumulus cloud particles on the incident light are negligible compared with that of smoke.

The phase functions of dust have a peak in the forward-scattering direction. But the peak is not as strong as the case of cumulus cloud. The level of the scattering effects of dust is between that of smoke and cumulus cloud.

As mentioned before, phase functions (PDFs of scattering angle θ) and absorption probability P_{abs} only describe the photon-particle interaction for a single scattering event. However, in general, multiple-scattering events happen before photons reach the medium edge. In each scattering event, independent random variables θ and d are generated based on their PDFs, respectively. If a photon is not absorbed at the scattering event, the generated values prescribe the path of the photon up to the next scattering. The following chapter discusses the model of ray tracing for the multiple-scattering case.

Chapter 3

Model of ray tracing

3.1 Introduction

As stated in Chapter 2, a light pulse transmitted through the medium consists of numerous photons. The effects of the light propagating through the medium can be treated as the average outcome of the photon-particle interaction. When a photon encounters a particle (a scattering event happens), it is either absorbed by the particle or scattered away in a new direction. If the photon is not absorbed, the photon continues traveling through the medium up to the next scattering event. Typically, multiple scatterings occur before the photon reaches the medium edge. In each scattering, the independent scattering angle is generated based on the phase function, and the traveling distance between two consecutive scatterings is governed by exponential random variable d with mean D_{ave} . Thus, the direction of the path of the photon propagating through the medium may change in each scattering, and photons travel through a 3-D space.

In this chapter, a ray-tracing model of photons propagating through the scattering medium is developed. The axis rotation has to be done in each scattering in order to trace the position of photons in the 3-D space. The details of the axis rotation will be discussed in this chapter. Analysis of light signal dispersion presented in Chapter 5 is based on the ray-tracing model. Thus, the ray-tracing model is the core part of this thesis.

This chapter is organized as follows: Section 3.2 introduces three random variables, which coordinate a photon traveling through the 3-D space. The details of axis rotation algorithm are presented in Section 3.3. Conclusions are presented in Section 3.4.

3.2 Photons traveling through the 3-D space

Due to scatterings, the direction of the path of photons propagating through the medium may change in each scattering event. Photons travel through a 3-D space. In the ray-tracing model, it assumes that each scattering event is independent of each other.

There are three independent random variables d_n , θ_n and ϕ_n coordinating a photon traveling through the 3-D space [8, 10, 11, 12, 18]. The distance between two consecutive scatterings is an exponential random variable d_n with the PDF

$$p(d_n) = \frac{1}{D_{ave}} \exp\left(-\frac{d_n}{D_{ave}}\right). \quad (3.1)$$

The values of D_{ave} for cumulus cloud and battlefield particles are shown in Table-6.

Scattering angle θ_n is the angle between the direction of the incident path and that of the scattering path. The PDFs of scattering angle θ_n are called the phase functions, depicted by Figure 5.

Angle ϕ_n is introduced to account for photons traveling through the 3-D space. This angle defines the rotation of the scattering plane relative to the incident path, where the scattering plane is the plane including the incident path and the scattering path. It is a uniform random variable within the range of $[0, 2\pi]$.

At the n^{th} scattering point, the values of d_n , θ_n and ϕ_n are independently generated based on their PDFs. Moreover, each scattering event is independent of each other. Thus, $\{d_n\}$ are i.i.d (independent and identically-distributed) random variables, so are $\{\theta_n\}$ and $\{\phi_n\}$. These generated values determine the direction of the scattering path of the photon.

Figure 7 describes a trajectory of a photon as it travels through the 3-D space. Assume that the first scattering happens at point O_1 . A system of the rectangular coordinates x_1 , y_1 and z_1 is built with point O_1 as the origin. The x_1 , y_1 and z_1 rectangular coordinates are called the global coordinates. The n^{th} scattering point is represented as point O_n . The scattering path ($O_1 \rightarrow O_2 \rightarrow O_3 \dots$) is totally determined by the values of d_n , θ_n and ϕ_n generated in each scattering. The reference coordinates generating the values of d_n , θ_n and ϕ_n are the x_n , y_n and z_n coordinates, so the reference coordinates change in each scattering.

The purpose of ray tracing is to position the n^{th} scattering point O_n in the x_1 , y_1 and z_1 global coordinates: location information must be rotated to match the x_1 , y_1 and z_1 global coordinates. The rotation information is recorded in each scattering. The details of the axis rotation will be presented in the next section.

3.3 Axis rotation

In this section, the general rotation algorithm will be developed to trace the photons traveling through the 3-D space. As mentioned before, the first scattering happens at point O_1 . A system of rectangular coordinates (global x_1 , y_1 and z_1 coordinates) is built with point O_1 as the origin. See Figure 7 for a description. At point O_1 , the values of the three random variables d_1 ,

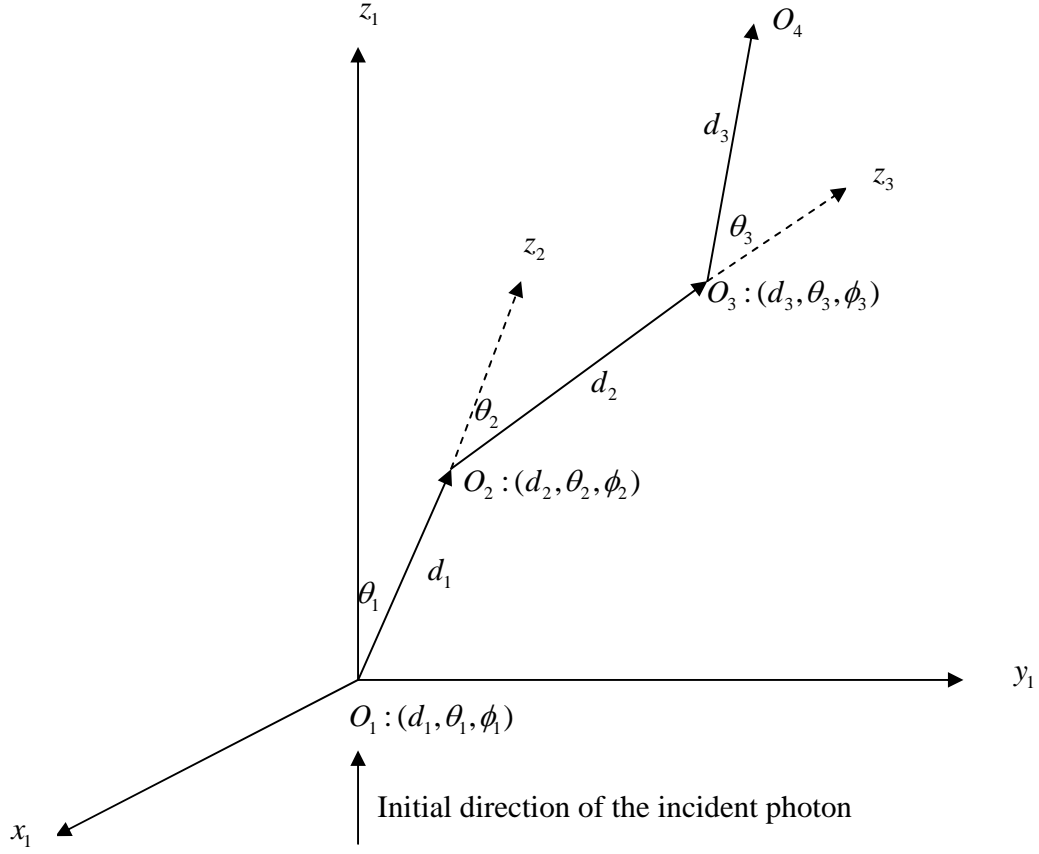


Figure 7. Description of the general rotation algorithm. The n^{th} scattering point is represented as point O_n . Coordinates x_1 , y_1 and z_1 are called the global coordinates.

$d_n = O_n O_{n+1}$: Distance between two consecutive scatterings.

θ_n : Angle between z_n axis and z_{n+1} axis.

ϕ_n : Angle between the rotation of the scattering plane relative to the incident path.

θ_1 and ϕ_1 are independently generated based on their PDFs. Then, the values prescribe the path of the photon up to the second scattering point O_2 if the photon is not absorbed. The values of the three random variables generated at point O_2 prescribe the scattering path after the second scattering if the photon is not absorbed at point O_2 . The direction of the scattering path continues to change as new scattering occurs. The position of scattering point O_n with reference to the x_{n-1} , y_{n-1} and z_{n-1} coordinates is known since the values of d_{n-1} , θ_{n-1} and ϕ_{n-1} are known. The purpose of the axis rotation algorithm is to position scattering point O_n in the x_1 , y_1 and z_1 global coordinates.

Before discussing the details of the algorithm of the axis rotation, parameter definitions and description of the rotation system will be presented in the following.

3.3.1 Parameter definitions

Below is a list of parameters of interest:

- x_n , y_n and z_n coordinates: the system of the rectangular coordinates. Point O_n is the origin of the x_n , y_n and z_n coordinates. It also represents the scattering point. The x_1 , y_1 and z_1 rectangular coordinates are called the global coordinates. Point O_1 , which refers to the first scattering point, is the origin of the global rectangular coordinates. The x_n , y_n and z_n coordinates in the case of $n \geq 2$ is called the local rectangular coordinates.
- θ_n : Angle between axis z_n and z_{n+1} .
- d_n : Distance between two consecutive scattering points O_n and O_{n+1} .

- ϕ_n : Angle is measured from the x_n axis in the $x_n - y_n$ plane.
- $\begin{bmatrix} x_{n-1}^n & y_{n-1}^n & z_{n-1}^n \end{bmatrix}$ when $n \geq 2$: the position of scattering point O_n in the x_{n-1} , y_{n-1} and z_{n-1} rectangular coordinates. In $\begin{bmatrix} x_{n-1}^n & y_{n-1}^n & z_{n-1}^n \end{bmatrix}$, lower symbol $n-1$ refers to the x_{n-1} , y_{n-1} and z_{n-1} rectangular coordinates; upper symbol n refers to scattering point O_n .

3.3.2 System description

- $\{d_n\}$: i.i.d random variables. The distribution is an exponential with mean D_{ave} shown in Table-6.
- $\{\theta_n\}$: i.i.d random variables. The distribution is the phase functions. See Figure 5.
- $\{\phi_n\}$: i.i.d random variables. The distribution is the uniform within the range of $[0, 2\pi]$.
- In each scattering event, random variables d_n , θ_n and ϕ_n are independent of each other. The reference coordinates generating the values of d_n , θ_n and ϕ_n are the x_n , y_n and z_n rectangular coordinates.

The position of scattering point O_n in the x_{n-1} , y_{n-1} and z_{n-1} coordinates is known. The purpose of the axis rotation is to position scattering point O_n in the x_1 , y_1 and z_1 global coordinates. In the following section, the details of the axis rotation are developed.

3.3.3 Rotation transformation

The rotation transformation of the point from the local rectangular coordinates to the global rectangular coordinates is described as

$$\begin{bmatrix} x_1^n & y_1^n & z_1^n \end{bmatrix}^T = Tr \begin{bmatrix} x_{n-1}^n & y_{n-1}^n & z_{n-1}^n \end{bmatrix}^T, \quad (3.2)$$

where Tr represents the transformation discussed as follows, and T represents the transpose of a vector. The following steps are taken to develop transformation Tr .

a) The second scattering point O_2 :

For the second scattering event, the position of point O_2 in the global rectangular coordinates is:

$$x_1^2 = d_1 \sin \theta_1 \cos \phi_1, \quad (3.3)$$

$$y_1^2 = d_1 \sin \theta_1 \sin \phi_1 \quad (3.4)$$

and

$$z_1^2 = d_1 \cos \theta_1. \quad (3.5)$$

b) The third scattering point O_3 :

For the third scattering event, the position of point O_3 in the global rectangular coordinates is:

$$\begin{bmatrix} x_1^3 & y_1^3 & z_1^3 \end{bmatrix}^T = R_z(\phi_1) R_y(\theta_1) \begin{bmatrix} x_2^3 & y_2^3 & z_2^3 \end{bmatrix}^T + \begin{bmatrix} x_1^2 & y_1^2 & z_1^2 \end{bmatrix}^T, \quad (3.6)$$

where $\begin{bmatrix} x_2^3 & y_2^3 & z_2^3 \end{bmatrix}^T$ is the position of scattering point O_3 with reference to the x_2 , y_2 and z_2 local rectangular coordinates. $R_z(\phi_1)$ and $R_y(\theta_1)$ are rotation matrices introduced to account for the axis rotation. The expressions of x_2^3 , y_2^3 and z_2^3 are obtained from

$$x_2^3 = d_2 \sin \theta_2 \cos \phi_2, \quad (3.7)$$

$$y_2^3 = d_2 \sin \theta_2 \sin \phi_2 \quad (3.8)$$

and

$$z_2^3 = d_2 \cos \theta_2. \quad (3.9)$$

The definitions of rotation matrices $R_z(\phi_1)$ and $R_y(\theta_1)$ are

$$R_z(\phi_1) = \begin{bmatrix} \cos \phi_1 & -\sin \phi_1 & 0 \\ \sin \phi_1 & \cos \phi_1 & 0 \\ 0 & 0 & 1 \end{bmatrix} \quad (3.10)$$

and

$$R_y(\theta_1) = \begin{bmatrix} \cos \theta_1 & 0 & \sin \theta_1 \\ 0 & 1 & 0 \\ -\sin \theta_1 & 0 & \cos \theta_1 \end{bmatrix}. \quad (3.11)$$

Since the position of the scattering point, $O_3 \begin{bmatrix} x_2^3 & y_2^3 & z_2^3 \end{bmatrix}$, is expressed with reference to the x_2 , y_2 and z_2 local coordinates, the local coordinates have to be rotated to obtain the position of scattering point O_3 with reference to the global coordinates. The rotation matrices $R_z(\phi_1)$ and $R_y(\theta_1)$ do this job.

c) The n^{th} scattering point O_n :

Accordingly, the position of n^{th} scattering point O_n with reference to the x_1 , y_1 and z_1 global rectangular coordinates are described as:

$$\begin{aligned} \begin{bmatrix} x_1^n & y_1^n & z_1^n \end{bmatrix}^T &= \left[\prod_{i=1}^{n-2} R_z(\phi_i) R_y(\theta_i) \right] \begin{bmatrix} x_{n-1}^n & y_{n-1}^n & z_{n-1}^n \end{bmatrix}^T \\ &+ \begin{bmatrix} x_1^{n-1} & y_1^{n-1} & z_1^{n-1} \end{bmatrix}^T, \end{aligned} \quad (3.12)$$

where $[x_{n-1}^n \ y_{n-1}^n \ z_{n-1}^n]^T$ is the position of scattering point O_n with reference to the x_{n-1} , y_{n-1} and z_{n-1} local coordinates. The expressions of the position of scattering point O_n with reference to the x_{n-1} , y_{n-1} and z_{n-1} local coordinates are

$$x_{n-1}^n = d_{n-1} \sin \theta_{n-1} \cos \phi_{n-1} \quad (3.13)$$

$$y_{n-1}^n = d_{n-1} \sin \theta_{n-1} \sin \phi_{n-1}, \quad (3.14)$$

and

$$z_{n-1}^n = d_{n-1} \cos \theta_{n-1}. \quad (3.15)$$

Next, taking Equation 3.10, 3.11, 3.13, 3.14 and 3.15 to Equation 3.12, one obtains

$$\begin{bmatrix} x_1^n \\ y_1^n \\ z_1^n \end{bmatrix} = \prod_{i=1}^{n-2} \begin{bmatrix} \cos \theta_i \cos \phi_i & -\sin \phi_i & \cos \phi_i \sin \theta_i \\ \sin \phi_i \cos \theta_i & \cos \phi_i & \sin \phi_i \sin \theta_i \\ -\sin \theta_i & 0 & \cos \theta_i \end{bmatrix} \begin{bmatrix} d_{n-1} \sin \theta_{n-1} \cos \phi_{n-1} \\ d_{n-1} \sin \theta_{n-1} \sin \phi_{n-1} \\ d_{n-1} \cos \theta_{n-1} \end{bmatrix} + \begin{bmatrix} x_1^{n-1} \\ y_1^{n-1} \\ z_1^{n-1} \end{bmatrix}. \quad (3.16)$$

Equation 3.16 describes the desired rotation transformation. If all the values of d_i , θ_i and ϕ_i generated in each scattering event are recorded, then the position of scattering point O_n with reference to the x_1 , y_1 and z_1 global rectangular coordinates can be obtained.

Equation 3.16 shows that the position of scattering point O_n with reference to the global coordinates depends not only on the values of θ_{n-1} , ϕ_{n-1} and d_{n-1} generated at the $(n-1)^{th}$ scattering point, but also the values of θ_i , ϕ_i and d_i generated previously, where $i = 1, 2, 3, \dots, n-2$. Since θ_i , ϕ_i and d_i are random variables, the global position of the scattering point, $O_n [x_1^n \ y_1^n \ z_1^n]$, is treated as a random vector, as well. Each component of this random vector is a function of θ_i , ϕ_i and d_i , where $i = 1, 2, 3, \dots, n-1$. Furthermore, the three components of the random vector strongly depend on each other.

The second term in the right side of Equation 3.16 describes the position of scattering point O_{n-1} with reference to the global coordinates. Therefore, this equation is a recursive equation. It is difficult to obtain analytic expressions of each component of random vector $\begin{bmatrix} x_1^n & y_1^n & z_1^n \end{bmatrix}$ when n is larger than 3.

3.4 Conclusions

Due to scatterings, the path of photons propagating through the scattering medium may change direction in each scattering. Photons travel through a 3-D space. A ray-tracing model is developed to trace photons propagating through the 3-D space. The purpose of ray tracing is to position the n^{th} scattering point O_n in the x_1 , y_1 and z_1 global coordinates. Axis rotation has to be done in order to trace the path of photons propagating through the 3-D space. Equation 3.16 is used to position the n^{th} scattering point O_n in the x_1 , y_1 and z_1 global rectangular coordinates.

Equation 3.16 is a recursive equation, and analytic expressions of scattering point O_n with reference to the global rectangular coordinates are difficult to obtain when n is larger than three. Computer simulations solve the problem.

In the next chapter, the model of computer simulations of the ray-tracing algorithm will be discussed. Computer simulations of each photon are performed individually, and then the sum of the data is used to develop a model of the entire transmission-particle medium interaction.

Chapter 4

Monte Carlo Ray Tracing (MCRT)

4.1 Introduction

In Chapter 3, the model of ray tracing of photons propagating through the 3-D space is developed. Since photons have numerous scatterings before reaching the medium edge and each scattering results in complicated trajectory changes, computer simulations are usually used to trace photons traveling through the 3-D space.

In this chapter, the Monte Carlo Ray tracing (MCRT) simulating photons propagating through the scattering medium is presented. Computer simulations of each photon are performed individually, and then the sum of the data is used to develop a model of the entire transmission-particle medium interaction. For computer simulations, it assumes that beam divergence of the light source is zero. Such an assumption is an abstraction to study the scattering effects of the medium independently of other factors. Moreover, it assumes that the transmitter and the receiver are both inside the scattering medium. Concepts of angular, spatial and temporal dispersion are introduced, as well.

This chapter is organized as follows. In Section 4.2, the details of the computer simulation model of ray tracing are presented. Spatial, angular and temporal dispersion of received photons are defined in this section, as well. Section 4.3 introduces two important parameters describing the physical size of the receiver: aperture size and field-of-view (FOV). Moreover, some concerns of the receiver design are discussed in this section. Finally, conclusions are presented in Section 4.4.

4.2 Model of computer simulations of ray tracing

Figure 8 shows a computer simulation scheme of ray tracing. It assumes that a cylinder lies within a homogeneous medium. A light source (transmitter) is placed at the origin of the x_1 , y_1 and z_1 coordinates. It also assumes that the light source is a point source, and the beam divergence of the light source is zero, so set $\theta_1 = 0$ and $\phi_1 = 0$. This is an abstraction to study the effects of the scattering medium independently of other factors. Lch represents the length of the LOS path along the optical axis of the transmitter; Lch also represents the medium length or the cylinder height. A circular plane with radius $5 \times Lch$ is placed at the $z_1 = Lch$ plane [10, 11, 12, 18]. The $5 \times Lch$ radius is an approximation for an infinite cloud—a cloud larger than the transmitter-receiver distance by far. This circular plane is called the receiver plane. Thus, the size of the cylinder is: the radius is $5 \times Lch$ and the height of it is Lch . Typically, the receiver is located at the center of the receiver plane to best receive the LOS photons. However, due to pointing error, the receiver may be at any location in the receiver plane. The physical size of the receiver is much less than that of the receiver plane.

It assumes that the light source ejects photons one by one to the optical channel. The initial direction of the transmitted photons is along the z_1 -axis. When a photon encounters a particle, a scattering event happens. The photon is either absorbed or scattered away onto a new course. The scattering path is totally determined by the values of d_n , θ_n and ϕ_n generated in each scattering event. When the photon passes through the receiver plane after multiple scatterings, the position of the passing point at the receiver plane is recorded. The passing point is represented as point D shown in Figure 8. In computer simulations, Equation 3.16 is used to trace the position of photons prorogating through the scattering medium.

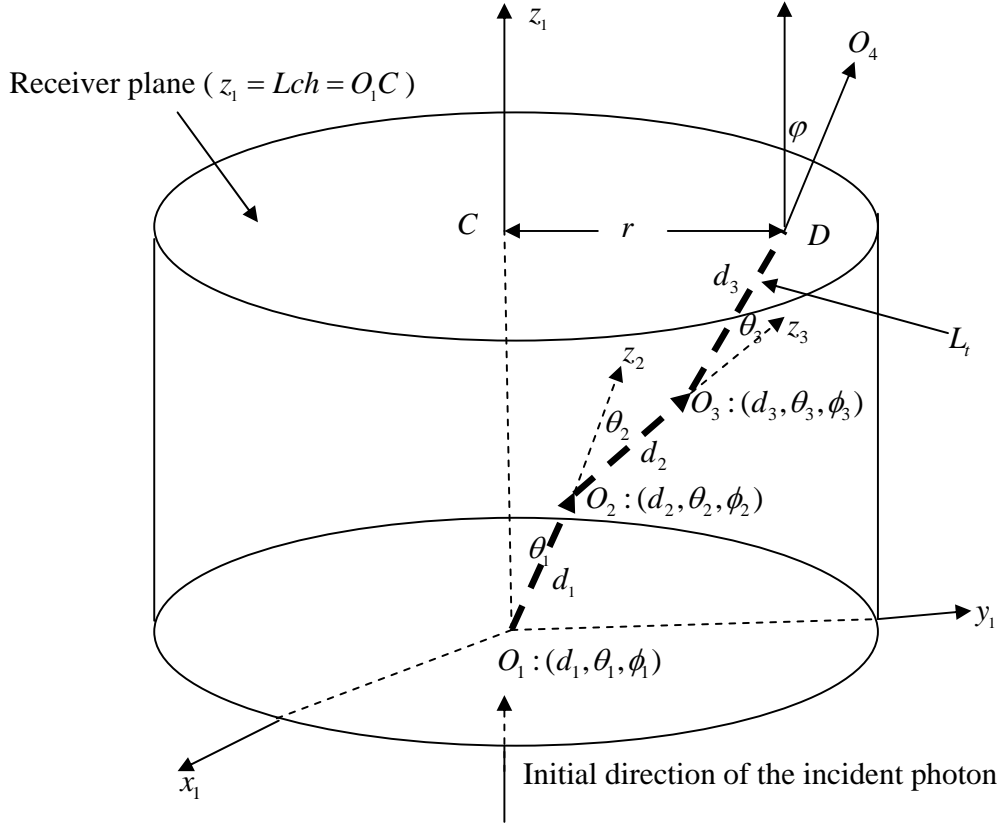


Figure. 8. A computer simulation scheme of ray tracing. The point light source is located at point O_1 . Beam divergence of it is zero, so set $\theta_1 = 0$ and $\phi_1 = 0$. The number of scattering events for the photon shown in the figure is two.

d_n : Distance between two consecutive scatterings.

θ_n : Angle between z_n and z_{n+1} axis.

ϕ_n : Angle between the rotation of the scattering plane relative to the incident path.

O_n : n^{th} scattering point.

D : Point that the photon passes through the receiver plane.

r : Spatial dispersion. φ : Angular dispersion.

L_t : Total traveling distance that a photon travels through the cylinder (bold dash line inside the cylinder: $L_t = O_1O_2 + O_2O_3 + O_3D$).

The computer records if the photons exit through the receiver plane or through the cylinder's sides, or if they are absorbed by the medium inside the cylinder.

When a certain number of photons pass through the receiver plane for a specific channel length, simulations terminate. Various properties of the photons passing through the receiver plane are then analyzed for a better reception result. For each photon received by the receiver plane, angular dispersion φ , spatial dispersion r , total traveling distance L_t and the number of scattering events that the photon propagating through the scattering medium are recorded. Figure 8 demonstrates a physical interpretation of angular, spatial and temporal dispersion of the received photons. The range of angular dispersion φ is $[0, \pi/2]$. The definition of temporal dispersion t_d is

$$t_d = \frac{L_t - Lch}{c}, \quad (4.1)$$

where parameter c is the speed of light.

The photons received by the receiver plane with zero spatial, angular and temporal dispersion are called the LOS photons. These photons travel along the optical axis of the transmitter (LOS path) and are not scattered at all. The number of the LOS photons, N_{LOS} , is recorded in simulations, as well.

The total number of transmitted photons N_t from the light source is calculated as

$$N_t = N_r + N_{loss}, \quad (4.2)$$

where N_{loss} is the number of the lost photons, and N_r is the number of the photons received by the receiver plane (not receiver). If a transmitted photon does not arrive at the receiver plane, then this photon is considered lost. The underlying causes of loss are basically absorption and scattering (photons passing through other sides of the cylinder rather than the receiver plane).

4.3 Parameters of the receiver

In this section, discussions of the model of the MCRT continue. As mentioned in Section 4.2, the physical size of the receiver will be much smaller than that of the receiver plane. Two parameters are commonly used to describe the physical size of the receiver: one is the receiver aperture size (radius) a , and the other is the field-of-view (FOV) half-angle ψ . Assume that a receiver is located at the center of the receiver plane. If the following two conditions are both satisfied

$$r \leq a \quad (4.3)$$

and

$$\varphi \leq \psi, \quad (4.4)$$

then photons with spatial dispersion r and angular dispersion φ are said to be received by the receiver.

In simulations, the energy of a light pulse received by the receiver is calculated as

$$E_r = \frac{N_r}{N_t}. \quad (4.5)$$

Generally, N_r consists of two parts

$$N_r = N_{LOS} + N_{scat}. \quad (4.6)$$

N_{scat} is the number of the received photons which will be subject to at least one scattering when they transverse through the medium. These photons are called the scattered photons. The LOS power caused by the LOS photons follows the Beer Lambert law [26]:

$$P_{LOS} = P_t \exp(-\tau), \quad (4.7)$$

where τ is optical thickness defined in Equation 2.19. From the above discussion, the received energy, E_r , is expressed as

$$E_r = E_{scat} + E_{LOS}, \quad (4.8)$$

where energy E_{scat} is caused by the received scattered photons, and is called the scattered energy.

Scattered energy E_{scat} is a function of the physical size of the receiver and pointing error BC .

Energy E_{LOS} is caused by the LOS photons, and is a function of optical thickness τ .

If a receiver is designed for collecting the LOS photons only, the bandwidth of the optical channel is enormous since temporal dispersion (pulse spread) of the LOS photons is zero. However, the LOS power follows an exponential decay. For a large value of optical thickness, a negligible LOS power is expected. For example, when $\tau = 17$, LOS power $P_{LOS} = -73.8dB$. Thus, in this situation, the receiver has to be designed to collect enough scattered energy to maintain the link availability.

Increasing the receiver aperture size and FOV will, in general, increase $N_{scat} (E_{scat})$. As a result, pulse spread Δt increases, which limits the data rate. The received peak power may also possibly reduce. See Equation 1.3. In addition, more background noise will be received due to large FOV. $N_{LOS} (E_{LOS})$ will not change at all since $N_{LOS} (E_{LOS})$ is a function of optical thickness. Thus, in FSOC, a receiver with a large FOV may not always provide benefits to the communications system. In Chapter 5, the relation among energy loss (E_r/E_t), the physical size of the receiver and pointing error BC will be investigated.

4.4 Conclusions

In the MCRT, it assumes that beam divergence of light source is zero and the transmitter and the receiver are both inside the scattering medium. Several phenomena cause energy loss in the FSOC channel link:

- Absorption loss: when the light signal is incident on particles, part of the incident light energy will be absorbed. Table-6 shows the probability of absorption P_{abs} for cumulus cloud and battlefield particles. Absorption probability P_{abs} is good for a single scattering event. If multiple scatterings are considered, the probability of photons absorbed by particles increases.
- Scattering loss L_s : when the light signal is incident on particles, part of the energy of the incident light will be scattered away to a new direction. The phase function describes the scattering effects for a single scattering event. The scattering effects cause spatial, angular and temporal dispersion of transmitted light signals. See Figure 8 for a description of dispersion. If the scattering effects are significant, so is scattering loss. Scattering loss includes two parts: energy loss and loss due to pulse spread Δt . See Equation 1.3.
- Free-space loss L_s : free-space loss is caused by non-zero beam divergence of the light source. Calculation of free-space loss is straight-forward. See Equation 1.2.

For some types of scattering media, loss caused by absorption is insignificant. For example, absorption probability P_{abs} of fog oil particles is 0.0073%. For such a small P_{abs} , loss caused by absorption is negligible compared to loss caused by scattering.

Due to the scattering effects, the photons received by the receiver plane consist of two parts (see Equation 4.6 and 4.8):

- LOS photons: these photons travel along the LOS path. These photons have desired properties: zero spatial, angular and temporal dispersion. However, the LOS power follows an exponential decay. See Equation 4.7. If a large value of optical thickness is of concern in FSOC, negligible LOS power will be received. Moreover, if a non-

zero value of point error is considered, the receiver may be totally outside the LOS area of the receiver plane. In this situation, only the scattered photons are collected, and a large value of pulse spread is expected.

- Scattered photons: photons are subject to at least one scattering when they transverse through the scattering medium. They do not have the properties of zero angular, spatial and temporal dispersion. In general, in order to catch more scattered photons, a receiver with the large aperture size and the FOV half-angle is suggested.

From the above discussion, when a large value of optical thickness is of concern, one way to maintain the link availability is to design a receiver to collect more scattered photons. However, the more scattered photons are collected, the more pulse spread is expected. As a result, the bandwidth of the optical channel and the peak power of the received light pulse may be reduced.

The following chapter investigates the relation among energy loss (E_r/E_t), receiver aperture size, FOV, and pointing error for cumulus cloud and fog oil particles. Receiver design issues are proposed based on the simulation results. Pulse spread caused by multiple-path effects is not considered.

Chapter 5

Computer simulation results and analysis

5.1 Introduction

As stated in Chapter 4, the received energy consists of two parts: the LOS energy and the scattered energy. See Equation 4.8. Once optical thickness is fixed, the LOS power is determined. See Equation 4.7. In general, in order to increase the received scattered energy, a receiver with a large aperture size and FOV half-angle is needed. In this chapter, the relation among energy loss (E_r/E_i), aperture size and FOV is investigated.

Moreover, the receiver can be located at any positions in the receiver plane if pointing error is considered. If the receiver is totally outside the LOS area, only the scattered photons are collected. Thus, energy loss is also a function of pointing error.

In this chapter, the computer simulations of ray tracing are used to investigate the property of spatial and angular dispersion of the received photons. The correlation between spatial and angular dispersion is investigated, which plays an important role in receiver design.

Cumulus cloud II and fog oil particles are selected for the computer simulations. The scattering effects of cumulus cloud II are much more significant than that of cumulus cloud I, since D_{ave} of cumulus cloud II is much smaller than that of cumulus cloud I. For the fixed channel length, the smaller D_{ave} is, the more scatterings happen when photons propagate through the non-absorption medium. See Equation 2.20. In order to consider the worst situation, cumulus cloud II is selected to run the computer simulations.

The simulation results of fog oil particles are quite predictive of the simulation results of the other smoke particles. Since the phase functions of smoke particles are similar, the simulation results on other smoke particles can be obtained by rescaling the simulation results of fog oil particles.

Several assumptions are made for the computer simulations:

- Only wavelength $1.55\mu m$ is considered.
- The beam divergence of the light source is zero.
- The transmitter and the receiver are both inside the scattering medium.

This chapter is organized as follows: In Section 5.2, the relation between energy loss and FOV is discussed when no pointing errors are introduced ($BC = 0$). The correlation of spatial and angular dispersion of the received photons is investigated in Section 5.3. Section 5.4 presents the property of the photon density distribution in the $x - y$ receiver plane. Receiver design issues for the two media are proposed in Section 5.5. Analysis of the simulation results of the two media is discussed in Section 5.6. Conclusions are presented in Section 5.7.

5.2 Relation between energy loss and FOV without pointing error ($BC = 0$)

In this section, it assumes that a receiver is located at the center of the receiver plane to best receive the LOS photons, so no pointing error is introduced. The aperture size of the receiver is assumed to be $10cm$ in radius and FOV half-angle is adjustable. Only optical thickness less than 17 is considered.

Figure 9, 10, 11, 12 and 13 demonstrate the relation between energy loss (E_r/E_t) versus FOV half-angle for the two scattering media. In order to catch more scattered energy, the

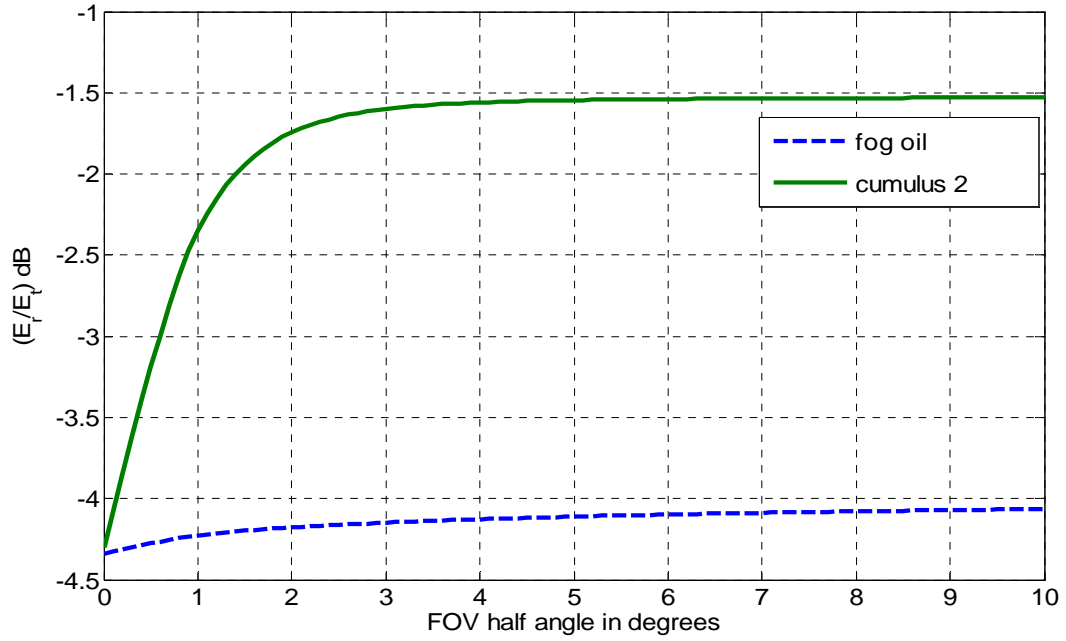


Figure 9. Energy loss versus FOV half-angle. Optical thickness $\tau = 1$ and aperture size is 10cm in radius.

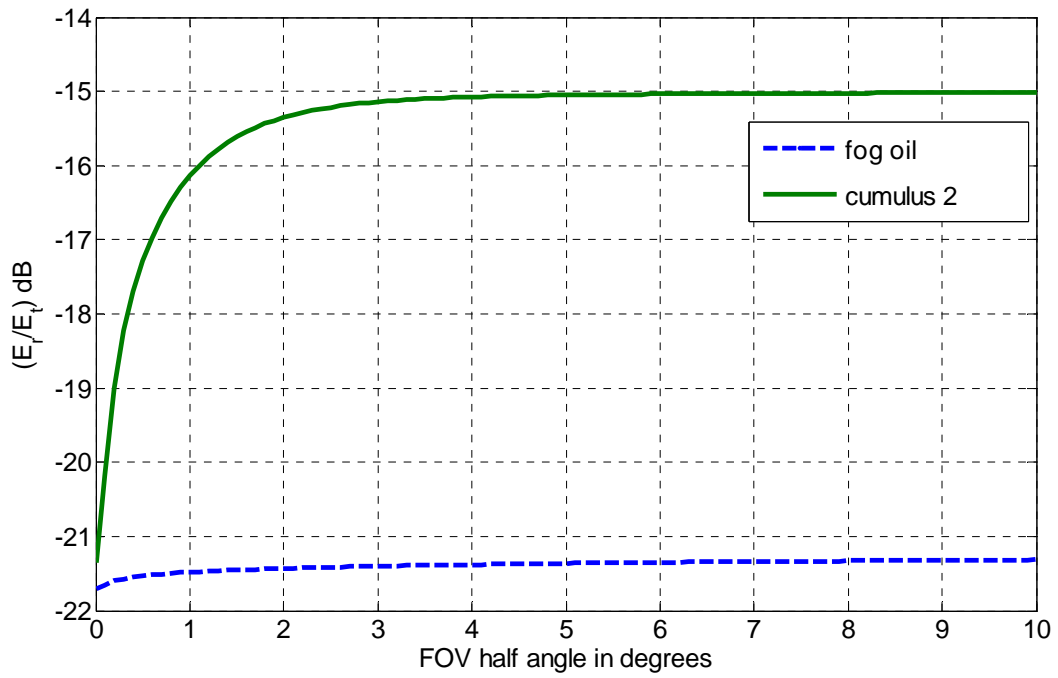


Figure 10. Energy loss versus FOV half-angle. Optical thickness $\tau = 5$ and aperture size is 10cm in radius.

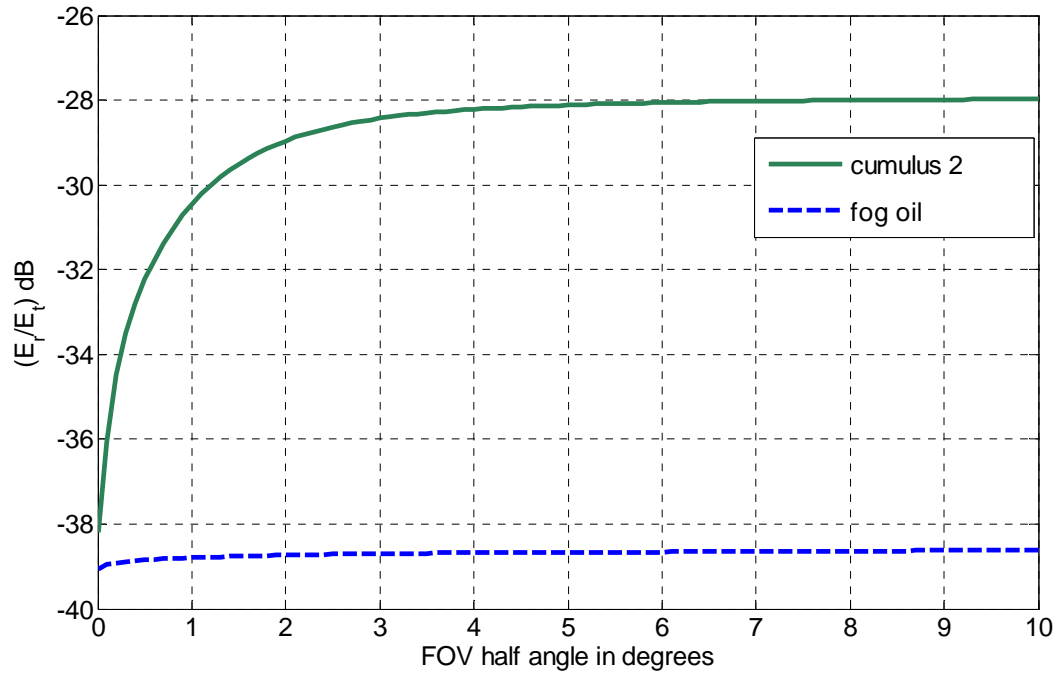


Figure 11. Energy loss versus FOV half-angle. Optical thickness $\tau = 9$ and aperture size is 10cm in radius.

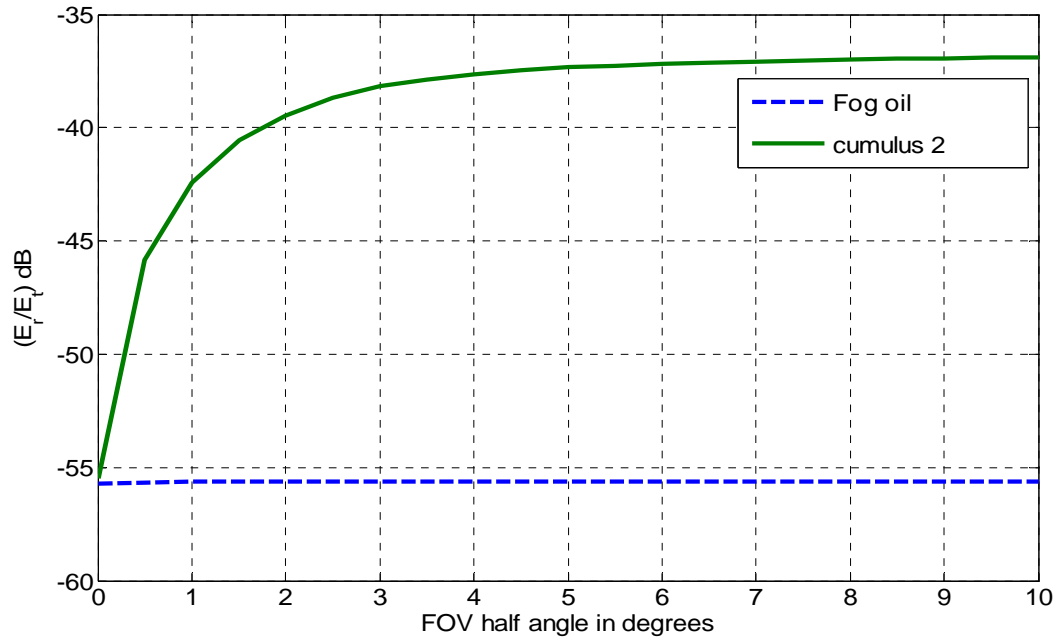


Figure 12. Energy loss versus FOV half-angle. Optical thickness $\tau = 13$ and aperture size is 10cm in radius.

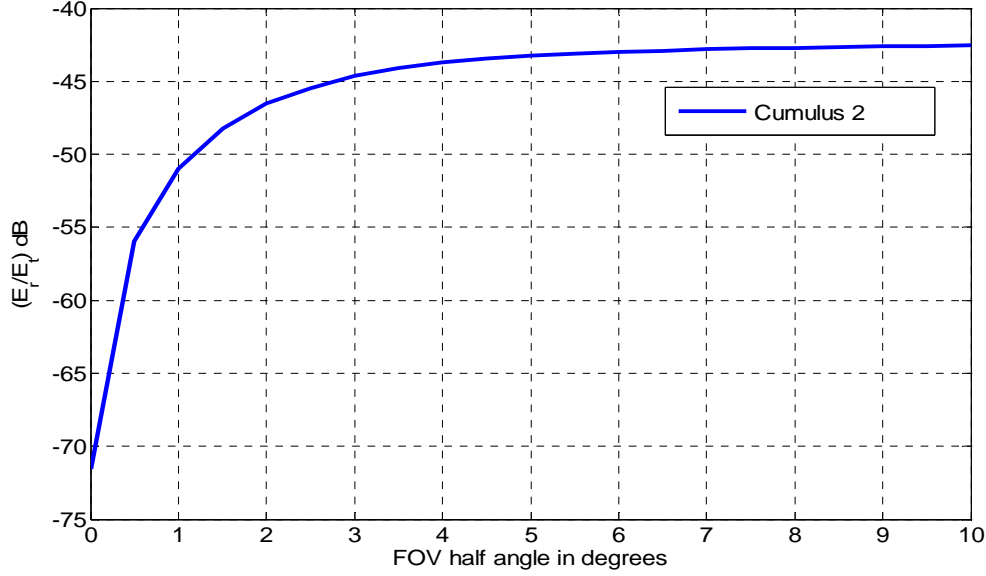


Figure 13. Energy loss versus FOV half-angle. Optical thickness $\tau = 17$ and aperture size is 10cm in radius. Only for cumulus cloud II.

FOV half-angle increases from zero to 10 degrees. Energy loss (E_r/E_t) for each FOV half-angle is calculated in units of dB . For optical thickness $\tau = 17$, only the simulation results for cumulus cloud II is shown.

For the fog oil medium, increasing the FOV half-angle does not help much to increase the received energy even if a large value of optical thickness is considered. Meanwhile, the energy received is mostly contribution of the LOS photons. Since pulse spread Δt of the LOS photons is zero, scattering loss L_s expressed by Equation 1.3 can be approximated as energy loss (E_r/E_t) .

However, for cumulus cloud II, the situation is completely different. Increasing the FOV half-angle helps much to increase the received energy, especially for a large value of optical thickness.

For all the simulation results discussed in this section, pointing error BC is assumed to be zero. However, in real applications, the receiver may not always be located at the center of the

receiver plane to best receive the LOS photons. Moreover, since the LOS power follows an exponential decay, the scattered photons play important roles in the receiver design when a large value of optical thickness is concerned. In the following section, the correlation of spatial and angular dispersion of the received photons distributed in the receiver plane is investigated. It shows that the correlation plays a significant role in the receiver design.

5.3 Property of spatial and angular dispersion of the received photons distributed in the receiver plane ($z_1 = Lch$)

This section investigates the property of spatial and angular dispersion of the received photons distributed in the receiver plane. In Chapter 4, it has been shown that if Inequality 4.3 and 4.4 are both satisfied, a photon with the specific values of spatial dispersion r and angular dispersion φ is said to be received by the receiver located at the center of the receiver plane. However, in a real system design, point error has to be considered. Here, assume that pointing error BC can not be larger than $2m$, so only the received photons with spatial dispersion less than $2m$ are considered.

The correlation between spatial and angular dispersion of the received photons is one of the major concern in receiver design. 2-D histogram of spatial and angular dispersion of the received photons is drawn in order to investigate the correlation.

The method of drawing the 2-D histogram is described as follows: the receiver plane ($z_1 = Lch$ plane) is divided into various rings as shown in Figure 14. Variable r (spatial dispersion) represents the radius of each ring, so the value of r is the distance between the center of the receiver plane and the ring. Figure 15 shows a ring with a radius r in the receiver plane.

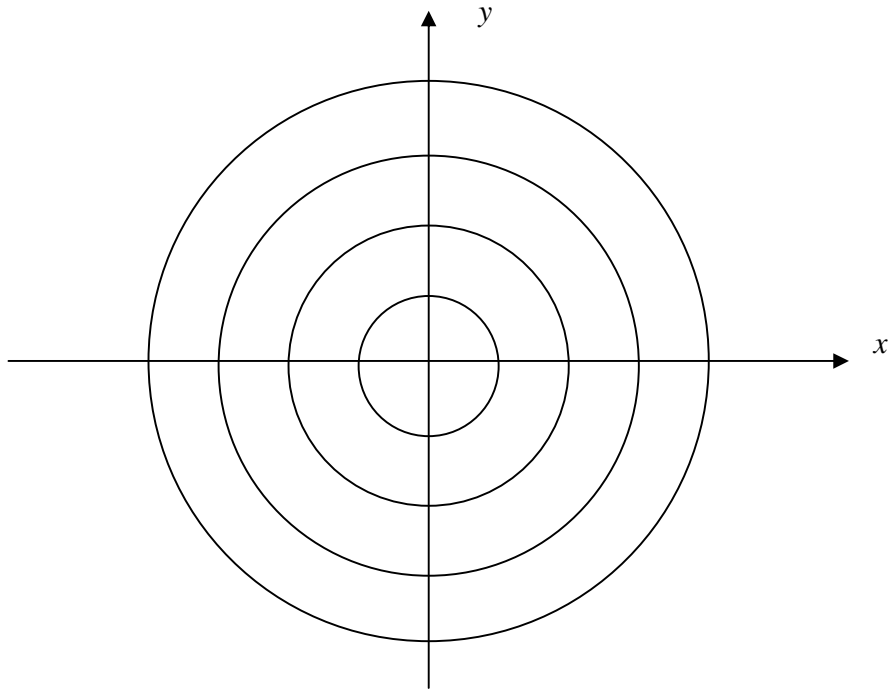


Figure 14. Scheme of the 2-D histogram of spatial and angular dispersion. The receiver plane is the $z_1 = Lch$ plane.

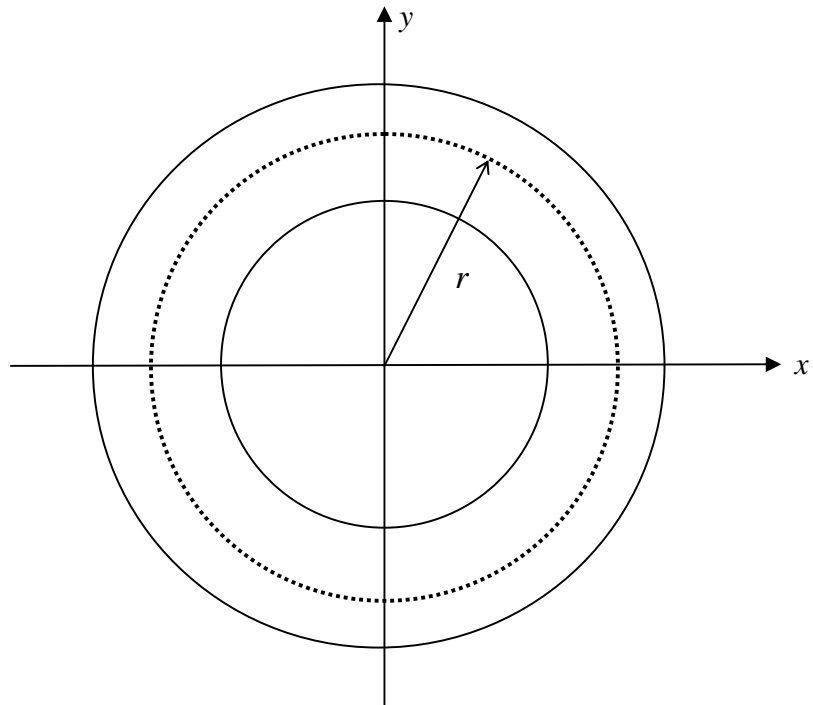


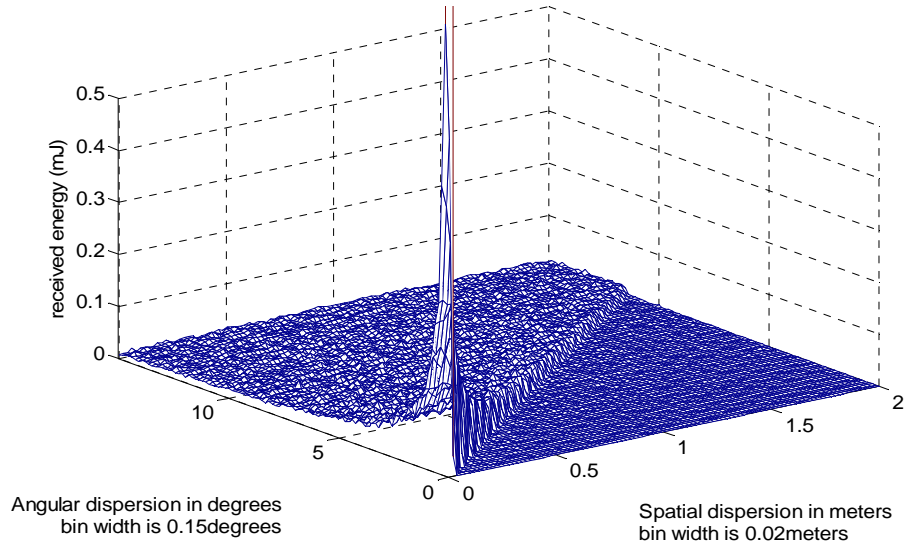
Figure 15. A ring with radius r in the $z_1 = Lch$ receiver plane.

The received photons inside each ring are sorted out, and then the histogram of angular dispersion of the received photons in each ring is calculated.

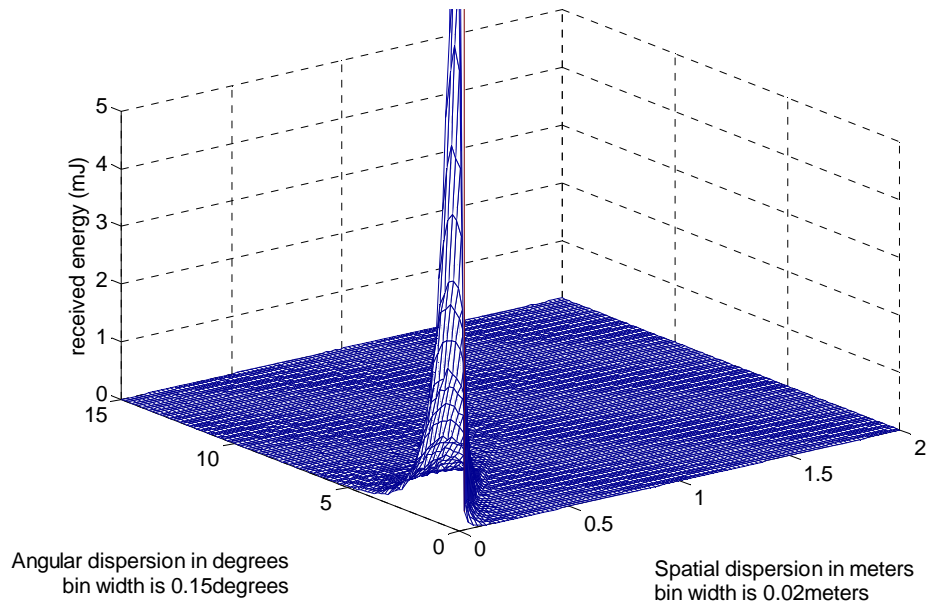
Figure 16, 17, 18, 19, and 20 show the 2-D histograms of dispersion of the received photons distributed in the receiver plane with spatial dispersion for the two scattering media $r \leq 2m$ ($BC \leq 2m$). Only simulation results of cumulus cloud II are shown in Figure 20. The scales of z -axis are adjusted in order to show the photon distribution outside the LOS area. Spatial dispersion from zero to two meters and angular dispersion from zero to ten degrees are demonstrated through these figures.

These figures are normalized so that the amplitude levels shown on the z -axis are compared to the total number of transmitted photons N_t . Thus, the ratio on the z -axis is the received energy when the transmitted energy is assumed to be one Joule.

For both media, when $\tau \leq 9$, all figures show a peak in the LOS area (the area with zero spatial and angular dispersion). This means that when a small value of optical thickness is concerned, the amount of the LOS energy is much more significant than that of the scattered energy. However, there are differences between the two media. Figure 16 (b), 17 (b) and 18 (b) show that a significant amount of the photons cluster around the LOS peak. These photons are the scattered photons. However, Figure 16 (a), 17 (a) and 18 (a) show that the amplitude of the scattered photons shown in the dispersion plane is negligible compared to that of the scattered photons for cumulus cloud II. For the fog oil medium, most of spatial dispersion of the scattered photons are larger than $2m$, which is not shown in the figures. It indicates that, for the fog oil, spatial dispersion of the received scattered photons is much larger than that of the received scattered photons for cumulus cloud II. For the fog oil medium, a negligible amount of the scattered photons cluster around the LOS peak.



(a) Fog oil



(b) Cumulus cloud II

Figure 16. 2-D histogram of spatial and angular dispersion of the received photons distributed in the receiver plane. $\tau = 1$.

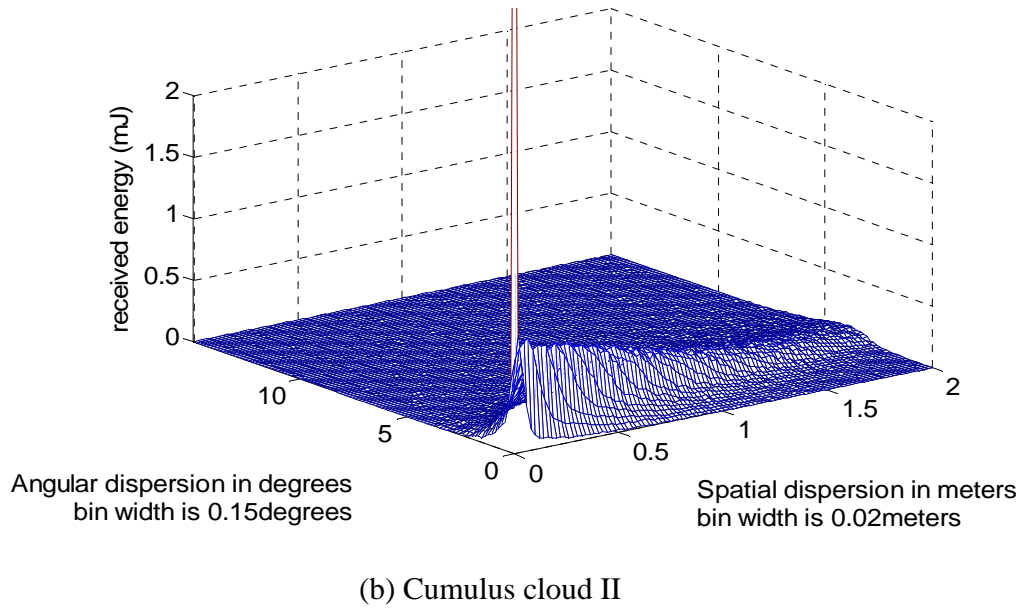
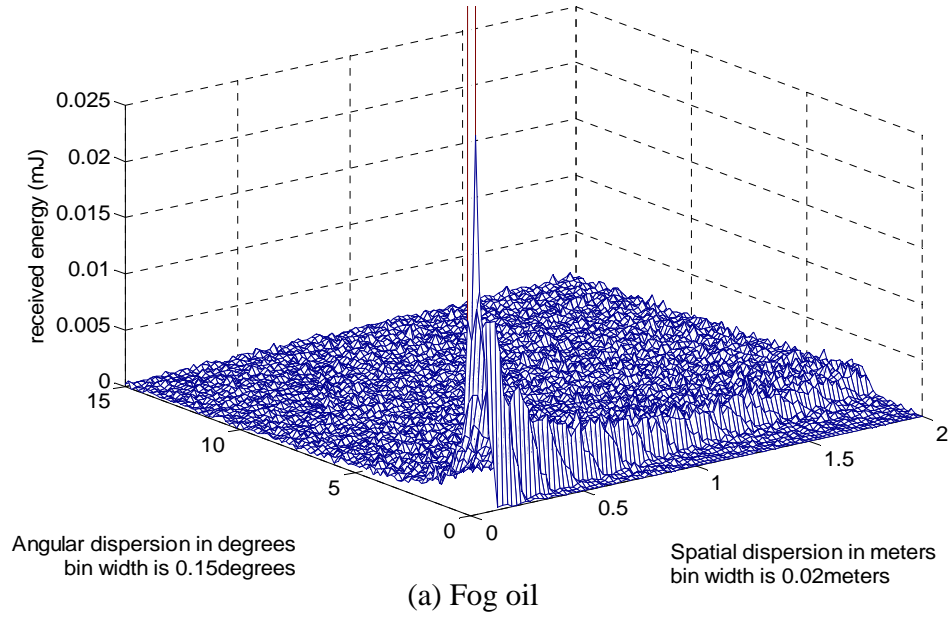
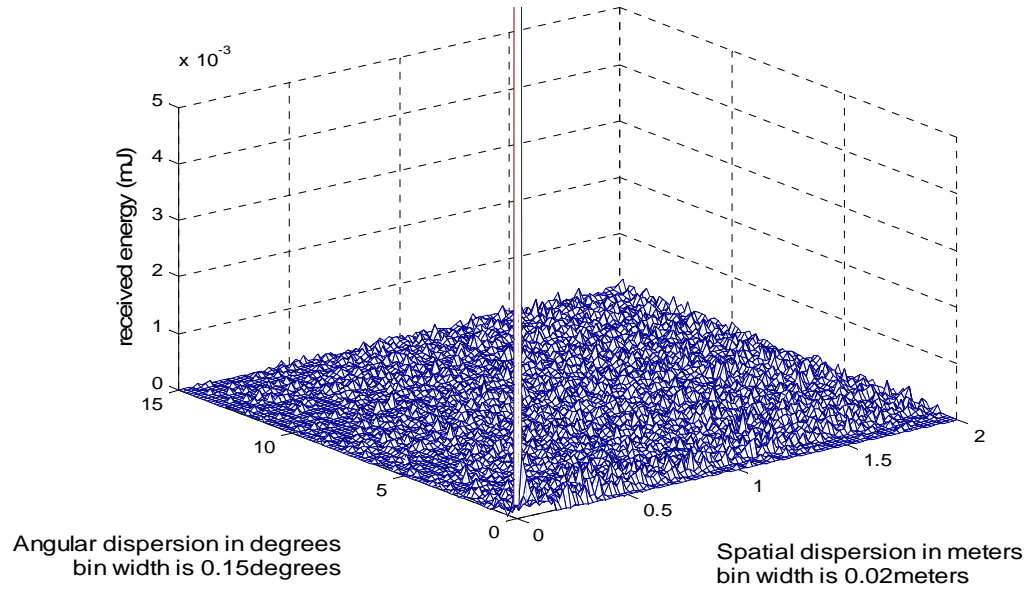
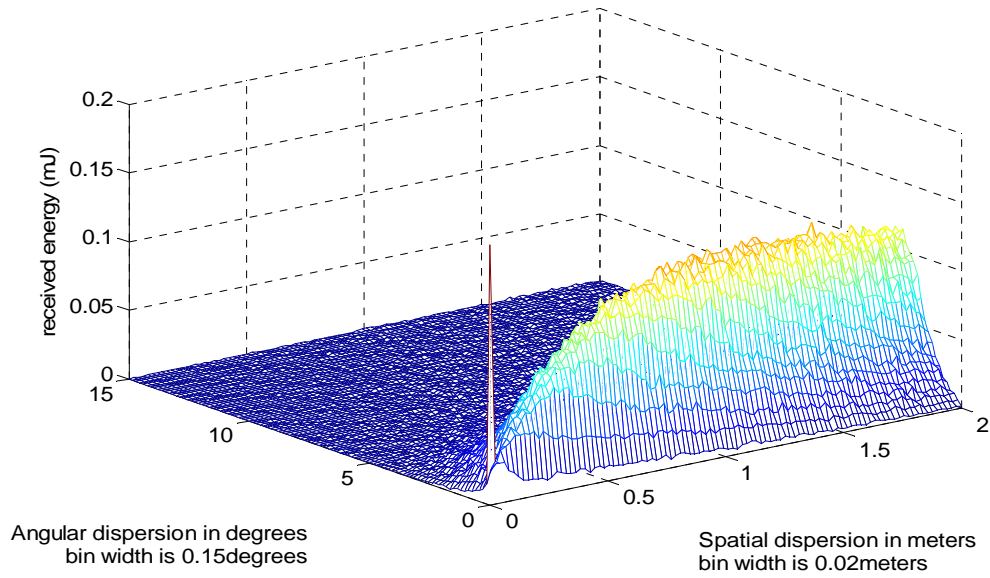


Figure 17. 2-D histogram of spatial and angular dispersion of the received photons distributed in the receiver plane. $\tau = 5$.

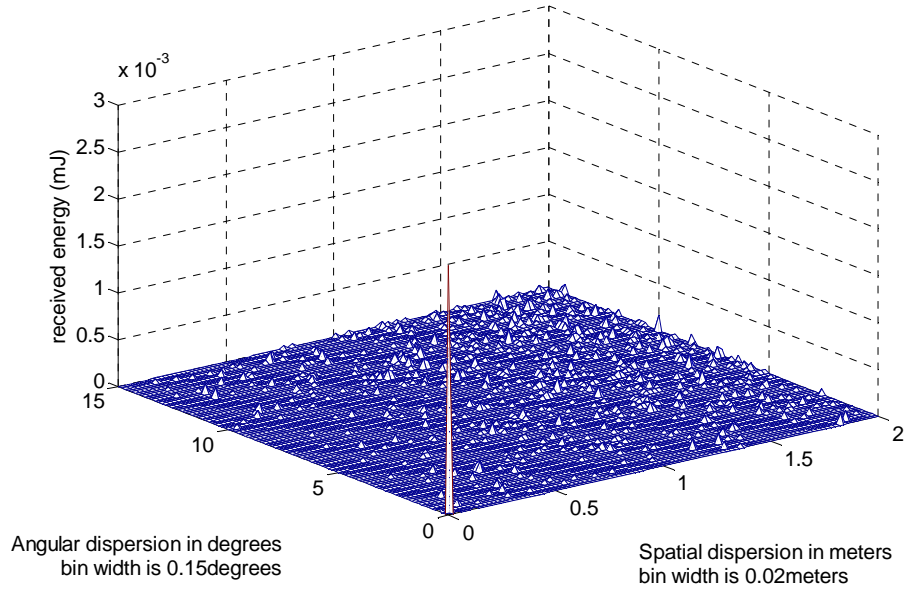


(a) Fog oil

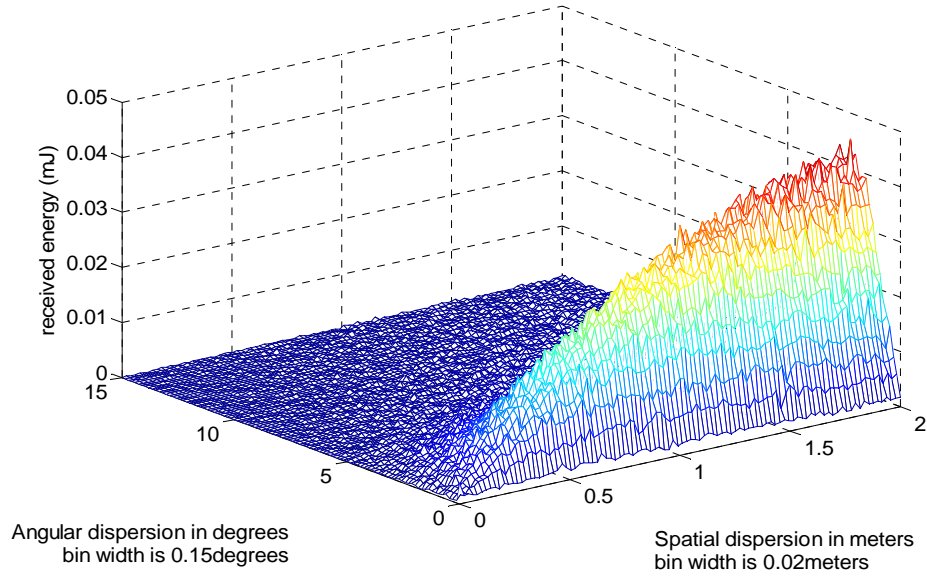


(b) Cumulus cloud II

Figure 18. 2-D histogram of spatial and angular dispersion of the received photons distributed in the receiver plane. $\tau = 9$.



(a) Fog oil



(b) Cumulus cloud II

Figure 19. 2-D histogram of spatial and angular dispersion of the received photons distributed in the receiver plane. $\tau = 13$.

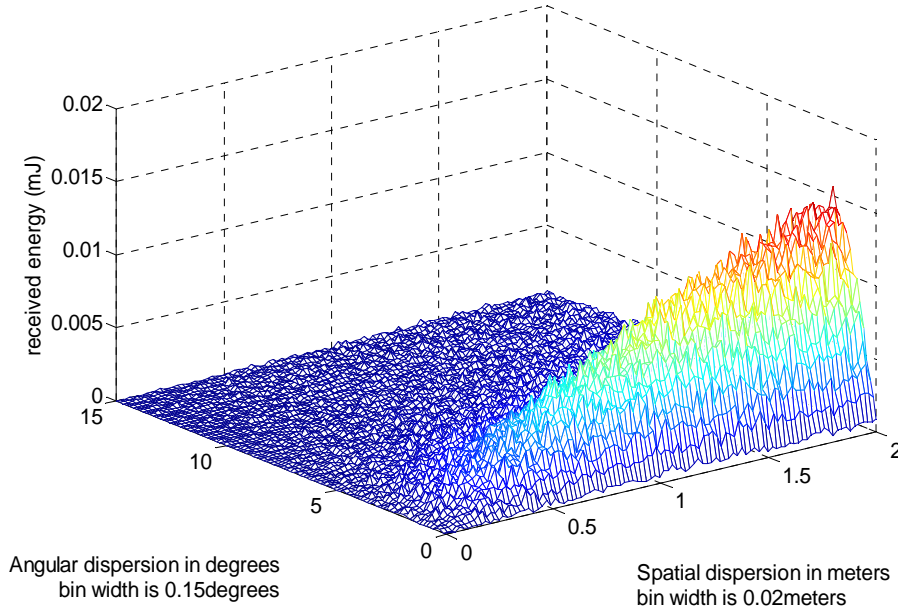


Figure 20. 2-D histogram of spatial and angular dispersion of the received photons distributed in the receiver plane. Cumulus cloud II; $\tau = 17$.

As optical thickness increases, the LOS energy follows an exponential decay, and the scattered energy caused by the scattered photons plays a more important role in the system design. However, since the scattering effects of fog oil particles are very significant, most of spatial dispersion of the received scattered photons is larger than $2m$. Thus, only the LOS photons causing the LOS power are meaningful to the system design regardless of the values of optical thickness. Therefore, for the fog oil medium, the receiver should always be located at the LOS area of the receiver plane to best receive the LOS photons. If the receiver misses the LOS photons due to pointing error or LOS attenuation is big (for a large value of optical thickness), then outage may occur since the amount of the scattered energy collected by the receiver is almost zero. For example, if a fog oil medium has a physical channel length of 200 meters, optical thickness of it is ~ 20 . The LOS attenuation is around $-87dB$. Moreover, the scattered

photons received by the receiver plane will have very large spatial dispersion, and most of the received scattered photons are far away from the LOS area of the receiver plane. Thus, the receiver located at the LOS area can only catch the LOS photons. For such a weak received power, the practical possibility of attaining optical communications through the fog oil medium would be impossible in this channel length.

Therefore, when a small value of optical thickness is concerned in FSOC, a receiver with a small FOV is proposed to find the LOS photons and work with them for both media. However, for cumulus cloud II in the case of a small value of optical thickness, even if a small value of pointing error exists, the communications link may still be available since there are a significant amount of the scattered photons clustered around the LOS peak, which is totally different from the case of the fog oil medium.

Figure 19 (b) and 20 show photons distributed in the dispersion plane for cumulus cloud II when a large value of optical thickness is concerned. Since the LOS power follows an exponential decay, the peak of the LOS photons significantly reduces. These figures show that the amplitude of the received energy increases along the axis of spatial dispersion. It merely indicates that more photons are received in a ring when radius r increases. The ring with a large radius r has a larger area than the ring with a small radius. Thus, it is possible that the number of the received photons in a ring with a large radius is more than the number of the received photons in a ring with a small radius. The two figures show that most angular dispersion of the received photons are less than 5 degrees when spatial dispersion is less than $2m$. As a result, the FOV half-angle of the receiver should not be more than 5 degrees to catch the scattered photons when pointing error BC is less than $2m$. Moreover, as shown in the two figures, the larger spatial dispersion is, the larger angular dispersion will be. If a receiver is intentionally placed

outside the LOS area ($BC > 0$), the FOV half-angle of the receiver should be larger than that of the receiver located at the LOS area in order to collect more scattered photons.

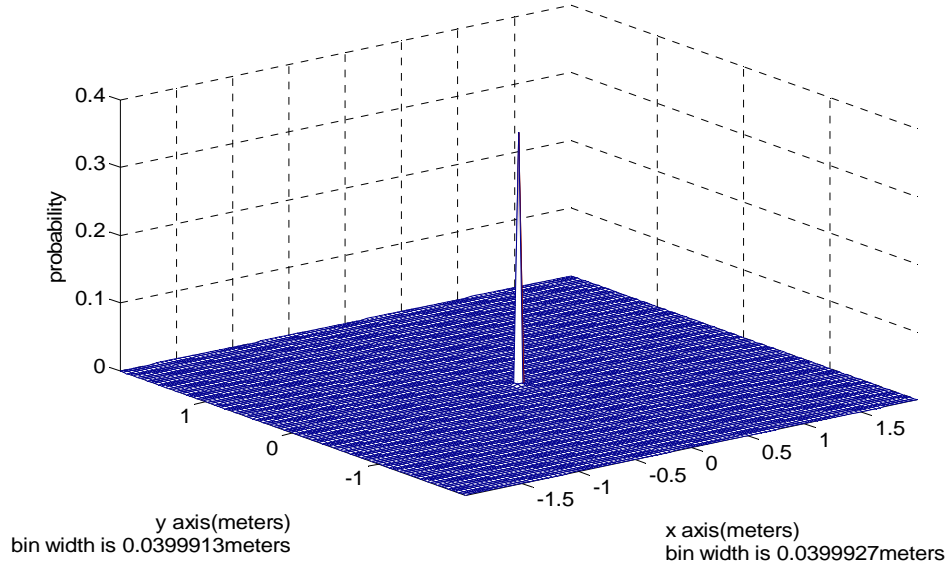
Accordingly, for cumulus cloud II, as far as a large value of optical thickness is concerned in FSOC, a receiver with a large FOV is needed to collect the scattered photons to maintain the link availability. Moreover, the FOV half-angle does not need to be more than 5 degrees if pointing error BC is less than $2m$.

The 2-D histograms shown in this section only illustrate the correlation between spatial and angular dispersion of the received photons distributed in the receiver plane. These figures do not illustrate the photon density distribution in the receiver plane ($x-y$ plane) due to the method of drawing the histograms. Moreover, the shape of the area of the receiver should be a circle rather than a ring. A ring with a large radius has more area. As mentioned before, it is possible that this ring will receive more scattered photons than the ring with a small radius. However, it does not mean that the receiver should be placed far away from the LOS area to collect the scattered photons.

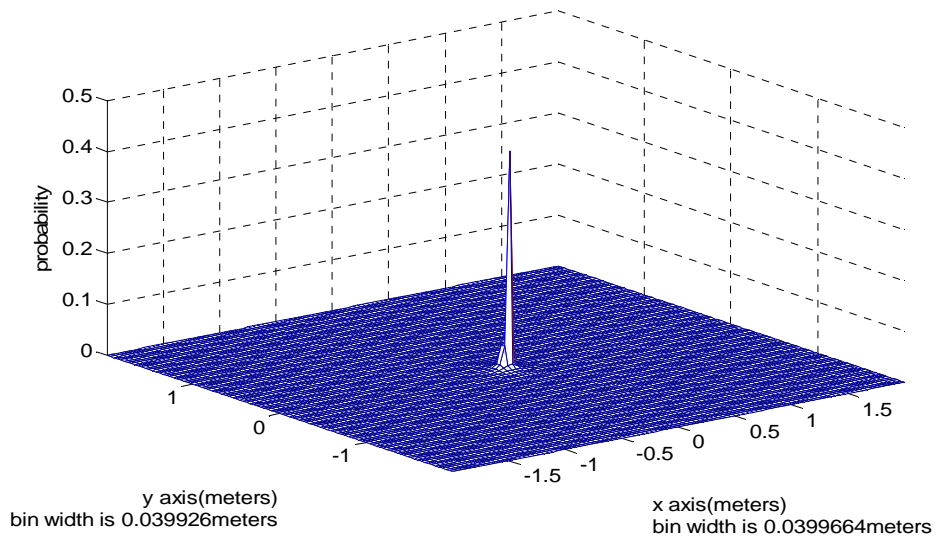
In the following discussion, the property of the photon density distribution in the receiver plane ($x-y$ plane) is investigated. As a result of this property, the best place where the receiver should be located can be found out for both media.

5.4 Property of the photon density distribution in the $x-y$ receiver plane

Figure 21, 22, 23, 24 and 25 show the photon density distribution in the $x-y$ receiver plane for both media. Optical thickness less than 17 is considered. Only received photons with spatial dispersion less than $2m$ are of concern. For optical thickness 13 and 17, only simulation results of cumulus cloud II are shown. Angular dispersion is not taken into account in these

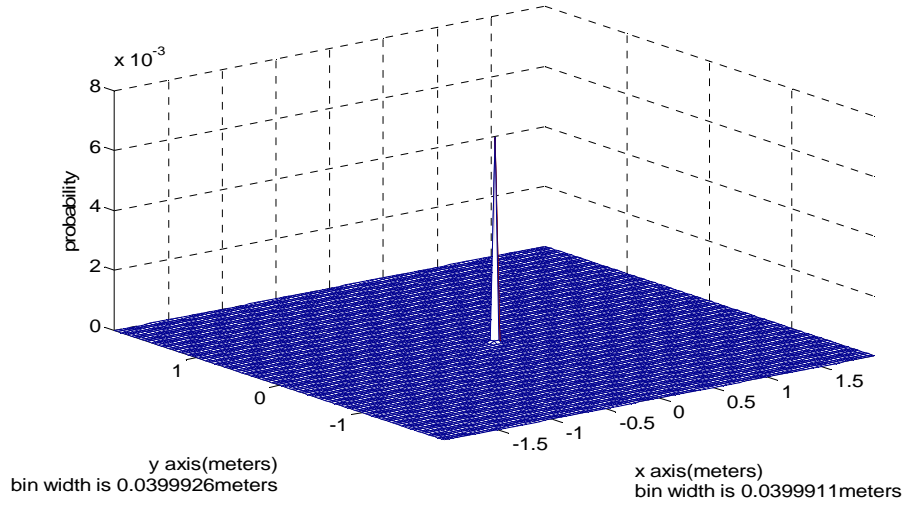


(a) Fog oil

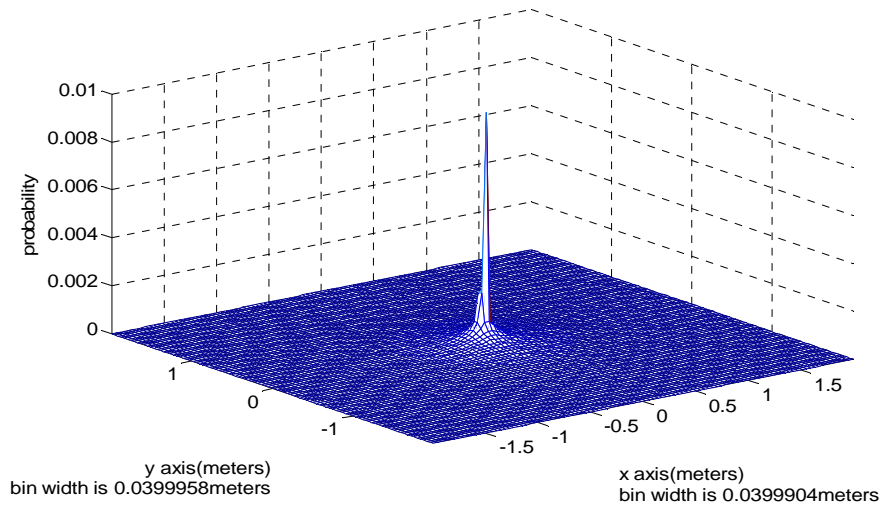


(b) Cumulus cloud II

Figure 21. Photon density distribution in the $x - y$ receiver plane. $\tau = 1$.

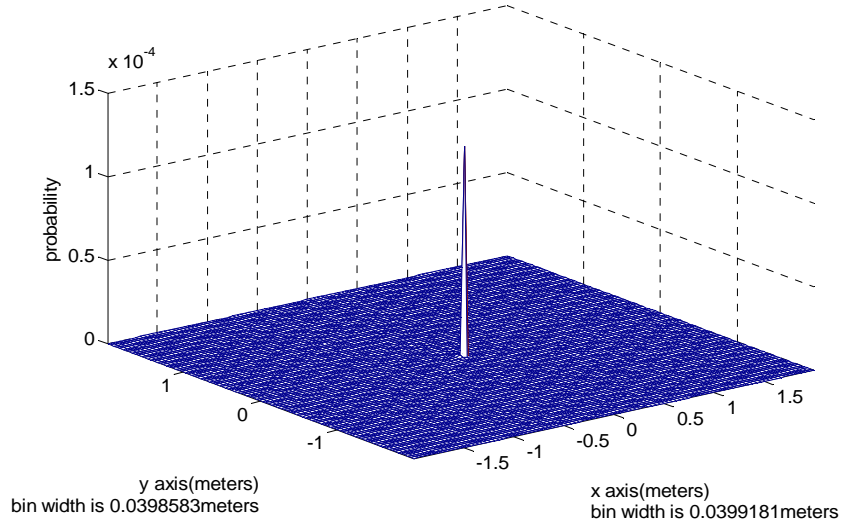


(a) Fog oil

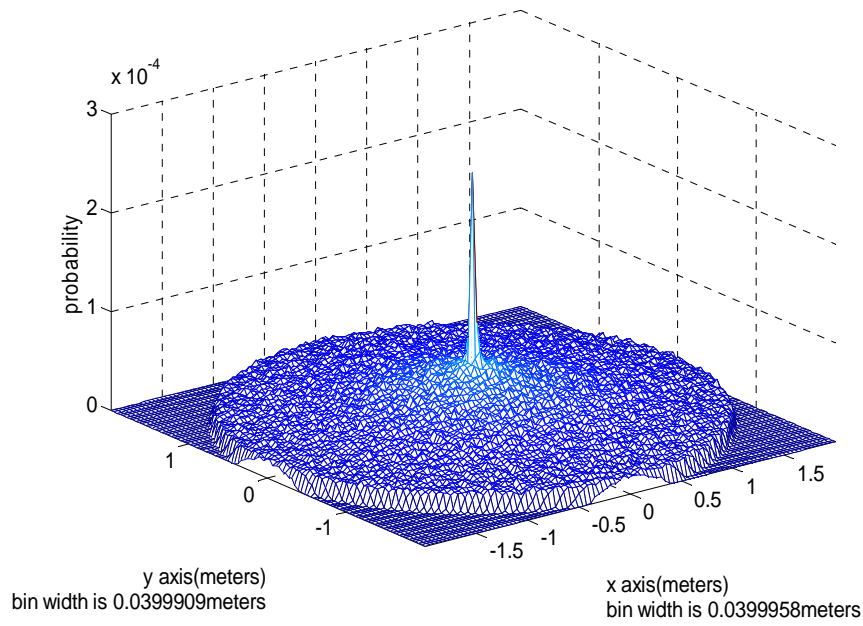


(b) Cumulus cloud II

Figure 22. Photon density distribution in the $x-y$ receiver plane. $\tau = 5$.



(a) Fog oil



(b) Cumulus cloud II

Figure 23. Photon density distribution in the $x - y$ receiver plane. $\tau = 9$.

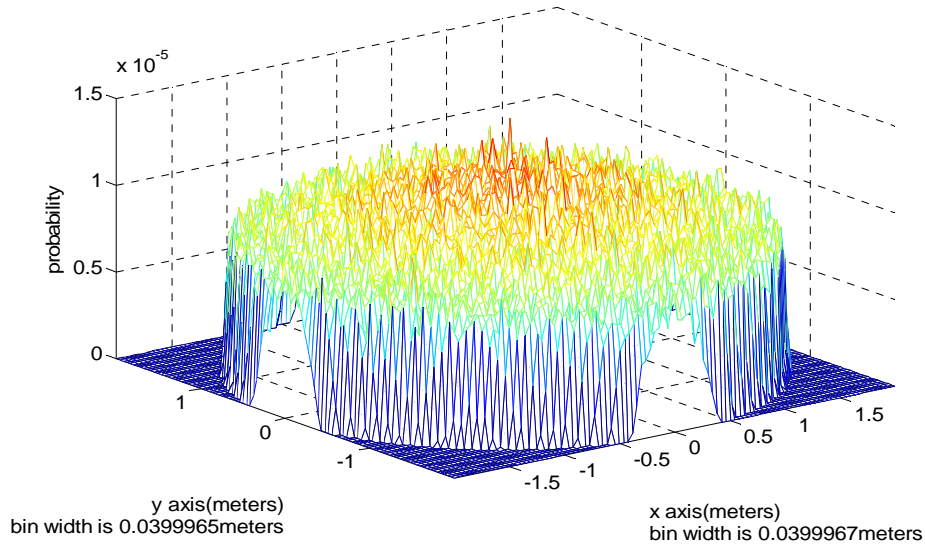


Figure 24. Photon density distribution in the $x - y$ receiver plane. Cumulus cloud II; $\tau = 13$.

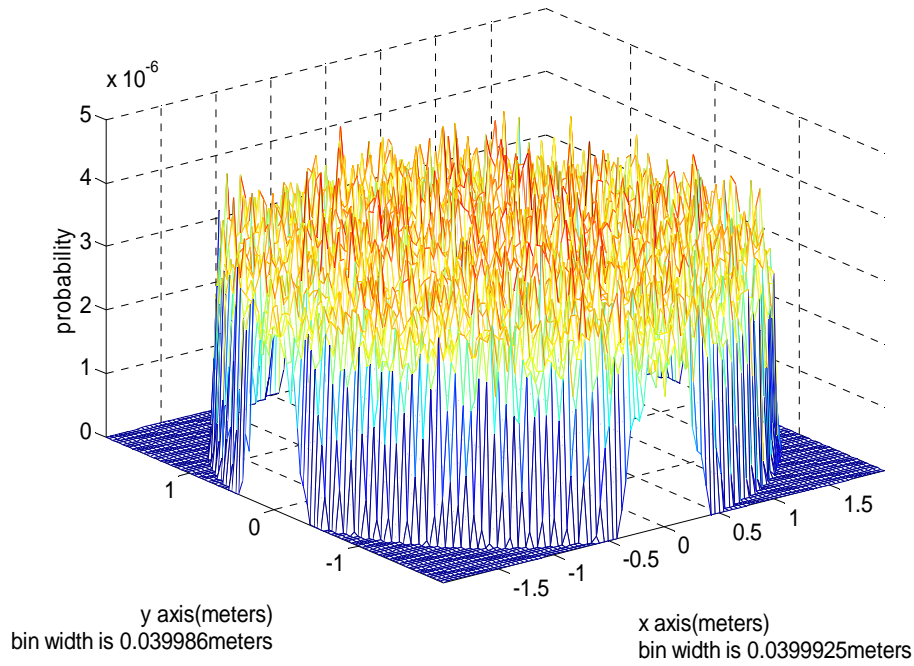


Figure 25. Photon density distribution in the $x - y$ receiver plane. Cumulus cloud II; $\tau = 17$.

figures. In other words, these figures indicate the energy density distributed in the $x - y$ receiver plane when spatial dispersion is less than $2m$. The amplitude levels shown on the z -axis are compared to the total number of transmitted photons N_t . Thus, the ratio on the z -axis can be treated as the probability of the arrived photons (energy density) in a specific area.

For a small value of optical thickness ($\tau \leq 5$), the photon density distributions in the $x - y$ receiver plane are similar for both media: there is a very strong peak in the LOS area of the receiver plane; the density of the photons distributed outside the LOS area is negligible compared to that of the photons distributed in the LOS area when spatial dispersion $r \leq 2m$. Thus, the LOS photons play an important role in the receiver design when a small value of optical thickness is concerned. However, there is a little difference between the simulation results of the two media. For the fog oil case, not so many photons clustered around the LOS peak. However, for the cumulus cloud II case, some photons clustered around the LOS peak. To best collect the received photons in the case of a small value of optical thickness, a receiver with a small FOV located at the center of the receiver plane is needed to find the LOS photons and work with them for both media.

For a large value of optical thickness ($\tau \geq 9$), the photon density distributions in the $x - y$ receiver plane are totally different for the two media. For the fog oil medium, there is only a peak located at the LOS area of the receiver plane: there are not much photons distributed outside the LOS area of the receiver plane when spatial dispersion $r \leq 2m$. Most spatial dispersion of the received photons is larger than $2m$, which are not shown in these figures. Thus, for the fog oil medium, only the LOS photons are meaningful to the receiver regardless of the values of optical thickness. If a pointing error is introduced, the energy received by a receiver with a specific physical size reduces dramatically.

The figures for cumulus cloud II show that a significant number of the photons clusters around the LOS peak when $\tau = 9$. Moreover, when $\tau \geq 13$, the amplitude of the LOS peak is comparable to that of the scattered photons, and the received photons are mostly uniformly distributed in the receiver plane when spatial dispersion $r \leq 2m$. Thus, for a large value of optical thickness ($\tau \geq 13$), even if a small pointing error is introduced ($BC \leq 2m$), the energy received by a receiver with a specific physical size may not change dramatically, which is different for the fog oil case.

In the next section, the issues in receiver design for both scattering media are discussed.

5.5 Receiver design for the two media

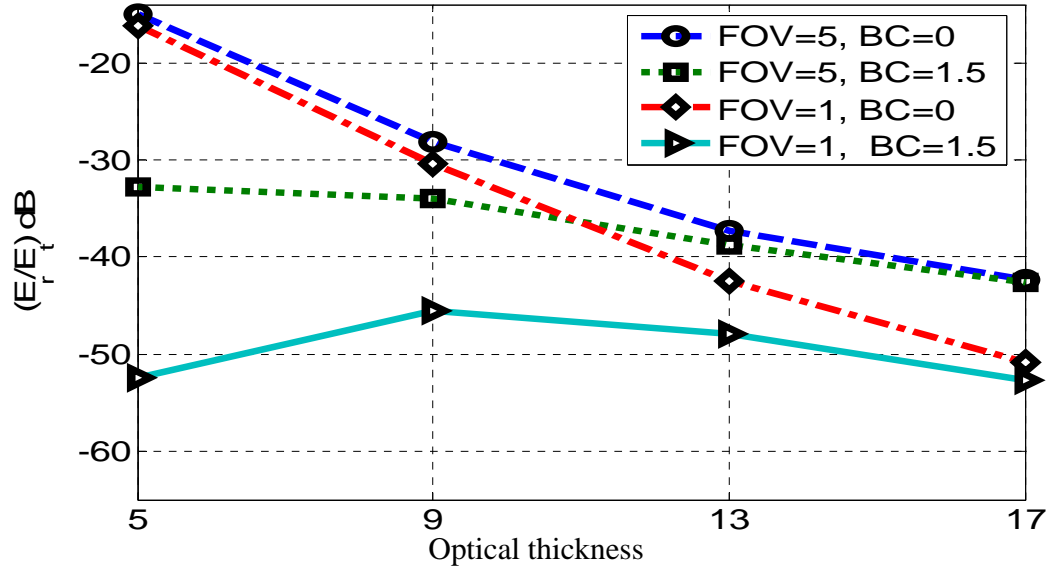
As mentioned in Section 5.3 and 5.4, for the fog oil medium, the receiver design is simple: a sensitive receiver with a small FOV is needed to find the LOS photons and work with them. Since only the LOS photons are meaningful for the system design, if a large value of optical thickness is concerned or pointing error is introduced, the receiver may not collect enough number of the received photons. As a result, an outage may occur.

However, for cumulus cloud II, the situation is different. When a small value of optical thickness is concerned in FSOC, a receiver with a small FOV is needed to catch the LOS photons and work with them. Even if a small pointing error is introduced, the receiver may still collect enough photons to maintain the link availability since there are some scattered photons clustered around the LOS peak. When a large value of optical thickness is concerned, a receiver with a large FOV is needed to catch the scattered photons. For a large value of optical thickness, the received photons are uniformly distributed in the receiver plane when spatial dispersion (pointing error) is less than $2m$. Since the LOS power follows an exponential decay, the received scattered

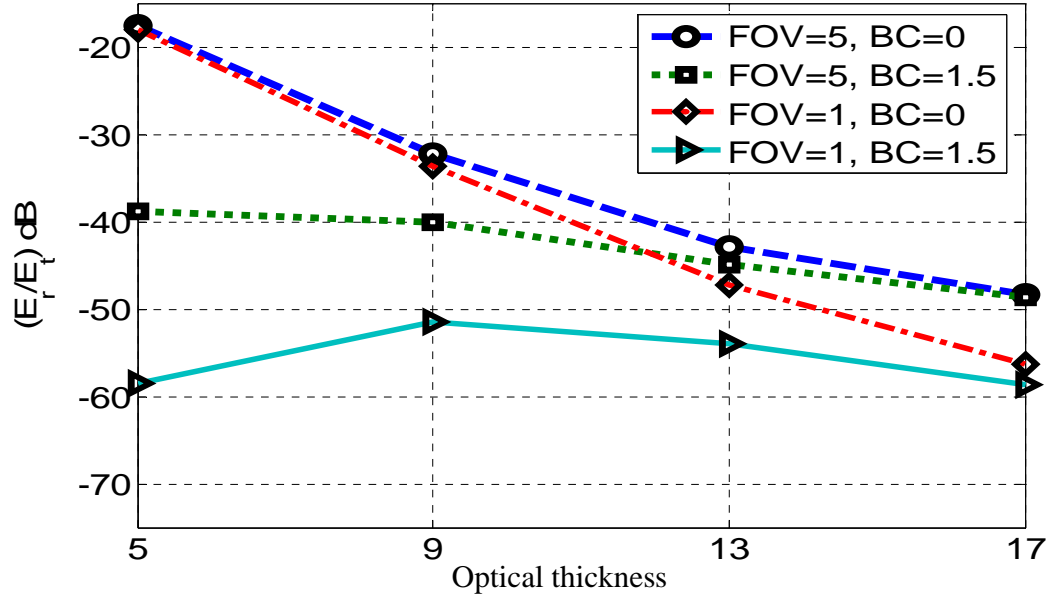
photons play important roles in the receiver design. A large FOV is proposed to collect more scattered photons to maintain the link availability. Moreover, for a large value of optical thickness, the number of the received photons collected by a receiver is not a function of pointing error if a small value of pointing error, $BC \leq 2m$, is considered.

Figure 26 shows energy loss (E_r/E_t) versus optical thickness with different values of BC and FOV half-angles. Only cumulus cloud II is considered. The simulation scheme is presented in Figure 27. See Figure 27 for the description of pointing error BC . An aperture size $10cm$ in radius is used in Figure 26 (a), and a smaller aperture size $5cm$ in radius is used in Figure 26 (b). The difference between the curves of $FOV=5^\circ$, $BC=0m$ and $FOV=1^\circ$, $BC=0m$ increases when optical thickness increases. It indicates that most angular dispersion of the received photons is less than 1 degree when optical thickness is small. However, when optical thickness increases, angular dispersion of the received photons increases, as well. A receiver with a large FOV is needed to collect the photons with large angular dispersion. Furthermore, the difference between the curves of $BC=0m$ and $BC=1.5m$ decreases when τ increases. This means that as long as $BC \leq 1.5m$ and τ is large, the receiver can collect the same order of the energy as the case without pointing error.

For cumulus cloud II, there are no preferred areas where a receiver should be located when a large value of optical thickness is concerned and $BC \leq 1.5m$. Therefore, when a large value of optical thickness is concerned in FSOC, multiple receivers may be placed at the receiver plane around the LOS area ($BC \leq 1.5m$) to increase the energy totally received. Figure 28 shows five receivers used to increase the received energy. Since photons are uniformly distributed in the receiver plane when spatial dispersion is less than $2m$, the total energy received by the five receivers will be five times the received energy for a single receiver.



(a) Aperture size 10cm in radius.



(b) Aperture size 5cm in radius.

Figure 26. Energy loss (E_r/E_t) versus optical thickness for different FOV half-angles and BC . Only for cumulus cloud II.

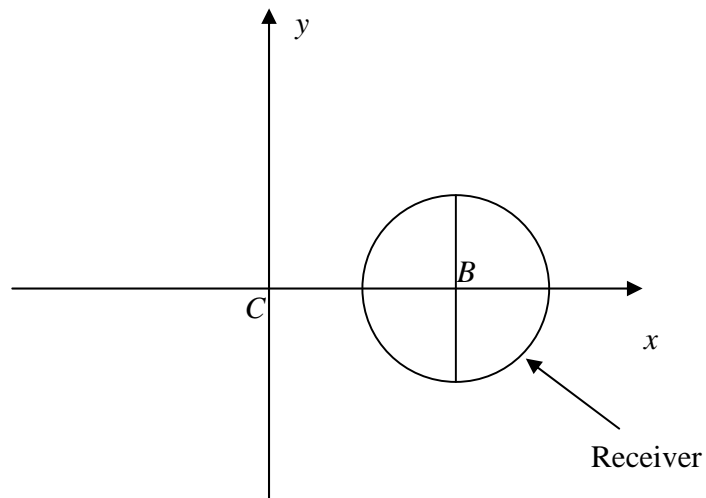


Figure 27. Simulation scheme for generating Figure 26.

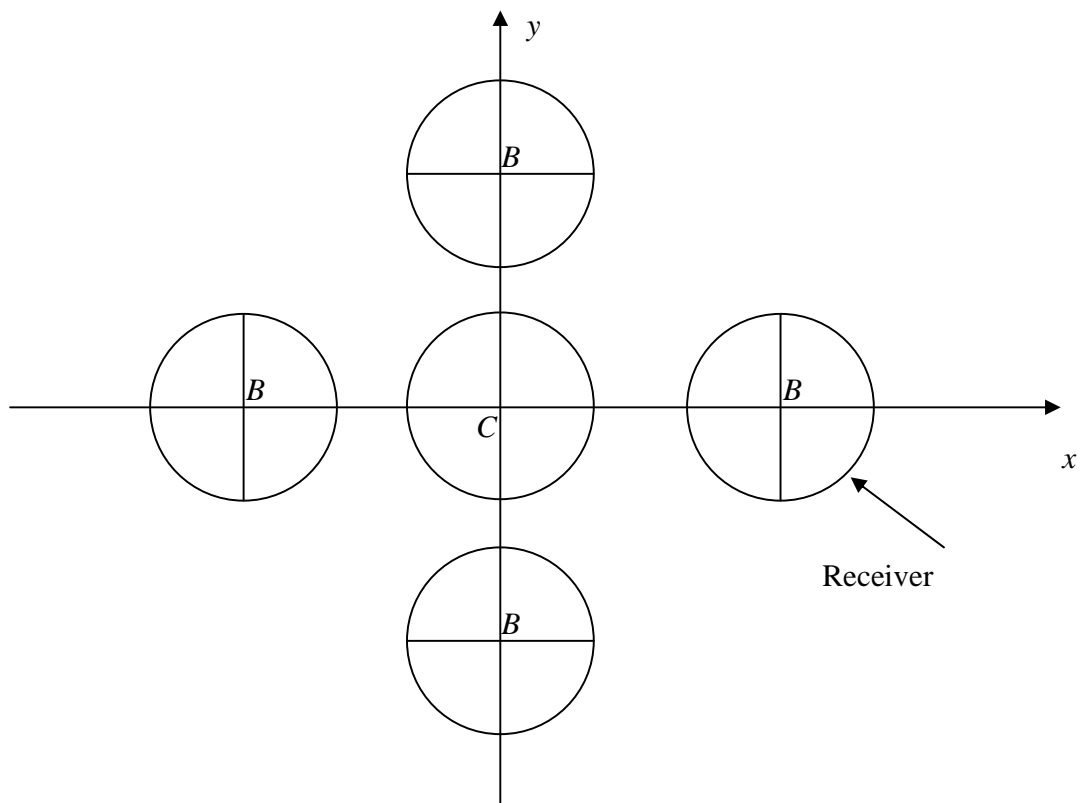


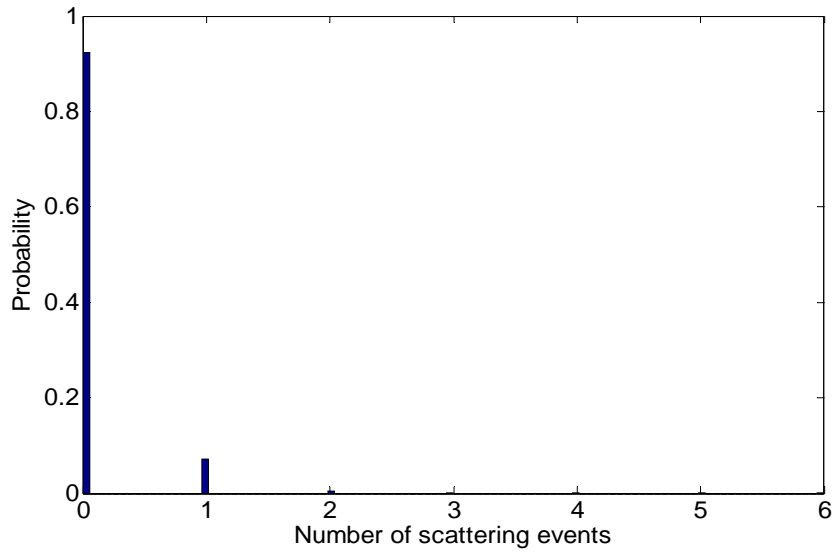
Figure 28. Multiple receivers located around the LOS area of the receiver plane.

It can be concluded that, for cumulus cloud II in the case of a large value of optical thickness, multiple receivers located around the LOS area are useful to maintain the link availability if BC is less than $2m$.

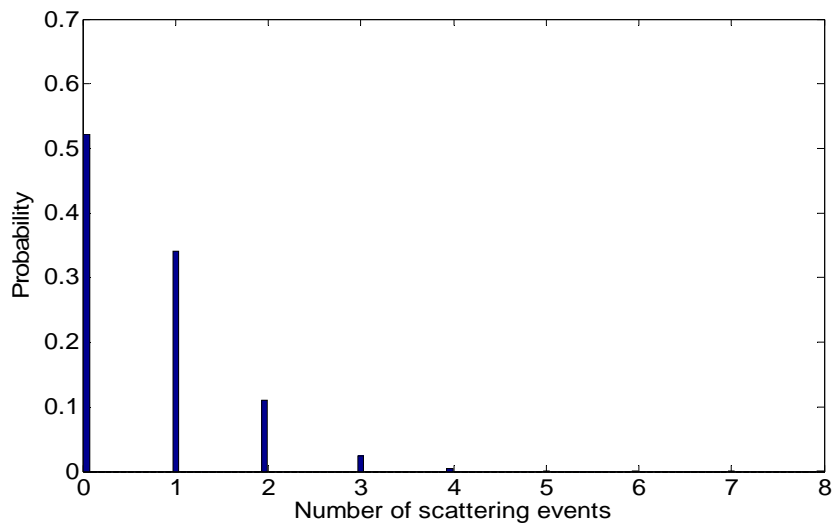
5.6 Analysis of computer simulation results for the two media

The histograms of the number of scattering events for the photons received by the receiver (not the receiver plane) with aperture size $10cm$ in radius and the FOV half-angle 90 degrees are shown in Figure 29, 30, 31, 32 and 33. Optical thickness less than 17 is considered. The receiver is assumed to be located at the center of the receiver plane. It shows that, in the fog oil case, most photons collected by the receiver are the photons with zero-scattering and one-scattering. In the case of cumulus cloud II, the mean of the number of scattering events can be approximated as optical thickness τ . Thus, most photons received by the receiver are the photons with multiple scatterings.

The simulation results for fog oil and cumulus cloud II particles can be explained by the physical properties of the two scattering media. The phase function of fog oil particles has no peak in the forward-scattering direction ($\theta = 0$) at all, and the mean of scattering angle θ is around 30 degrees, so the scattering effects of the particles on the incident light are significant. If a photon encounters a particle, the chance of the photon scattered away with a large scattering angle is high. For a photon received by the receiver plane (not the receiver), even if only one scattering event happens, the chance of the photon getting scattered far outside the LOS area of the receiver plane is high. When multiple scatterings are considered, the situation is much worse. A receiver located at the center of the receiver plane may never catch photons subject to at least



(a) Fog oil



(b) Cumulus cloud II

Figure 29. The histogram of the number of scattering events.

Aperture size (radius): 10cm ; FOV half-angle: 90 degrees; $\tau = 1$.

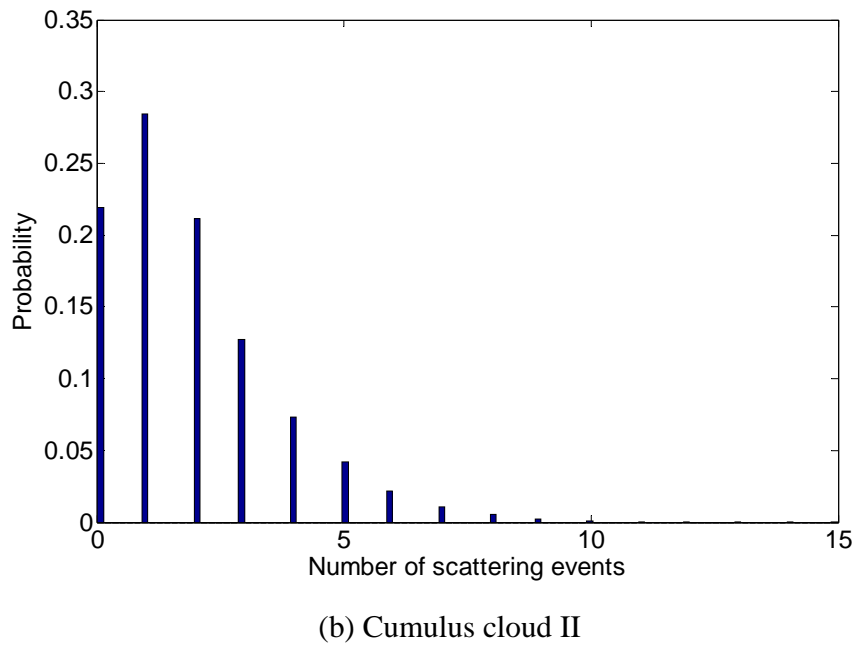
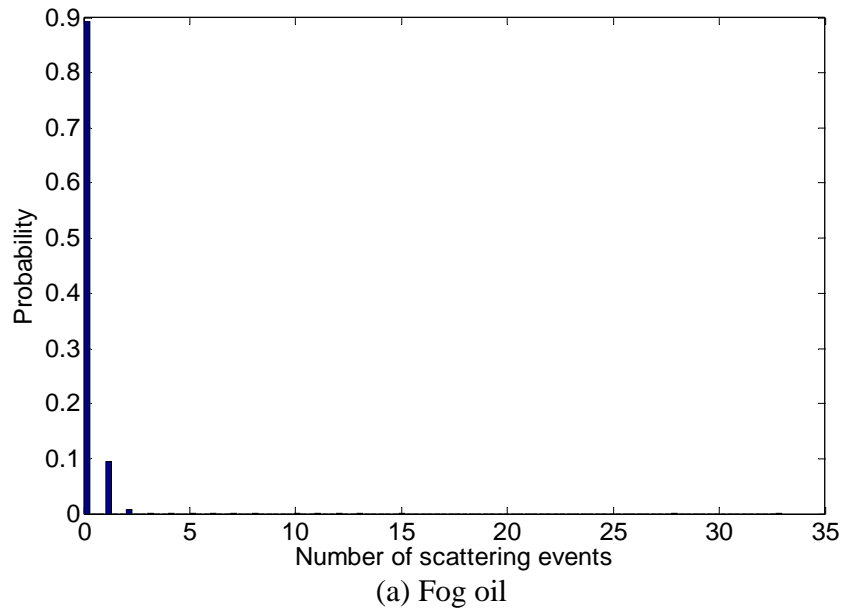
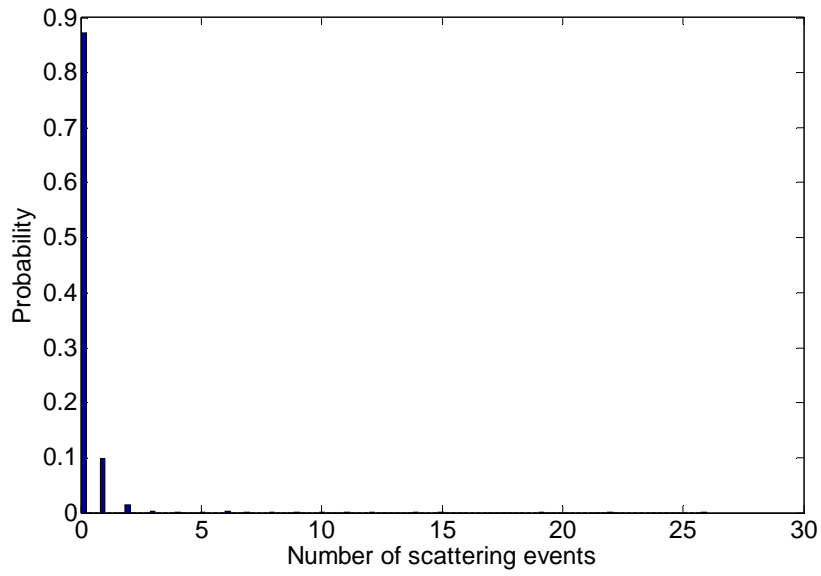
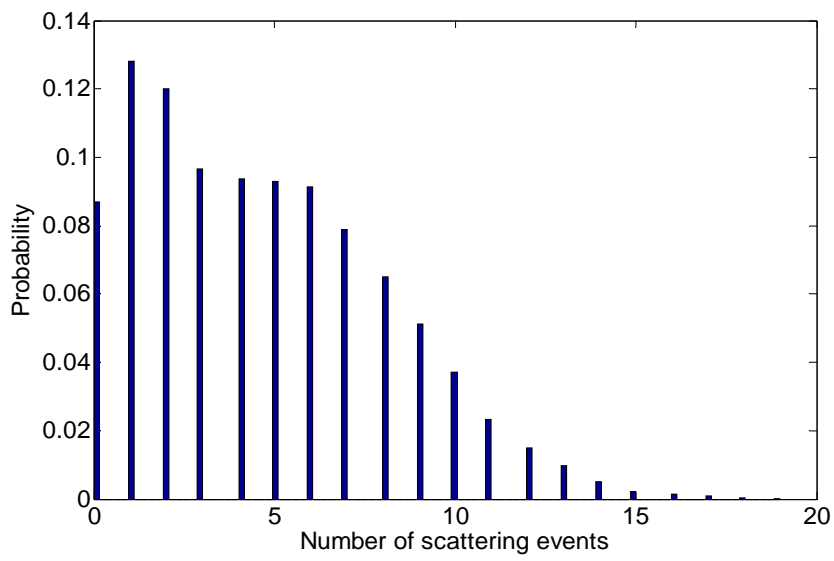


Figure 30. The histogram of the number of scattering events.

Aperture size (radius): 10cm ; FOV half-angle: 90 degrees; $\tau = 5$.



(a) Fog oil



(b) Cumulus cloud II

Figure 31. The histogram of the number of scattering events.

Aperture size (radius): 10cm ; FOV half-angle: 90 degrees; $\tau = 9$.

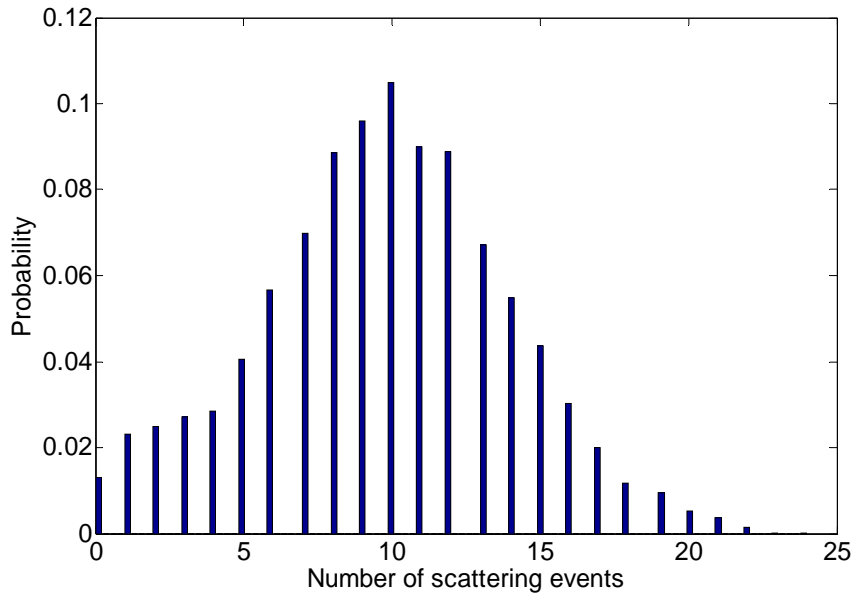


Figure 32. The histogram of the number of scattering events. Only for Cumulus cloud II.

Aperture size (radius): 10cm ; FOV half-angle: 90 degrees; $\tau = 13$.

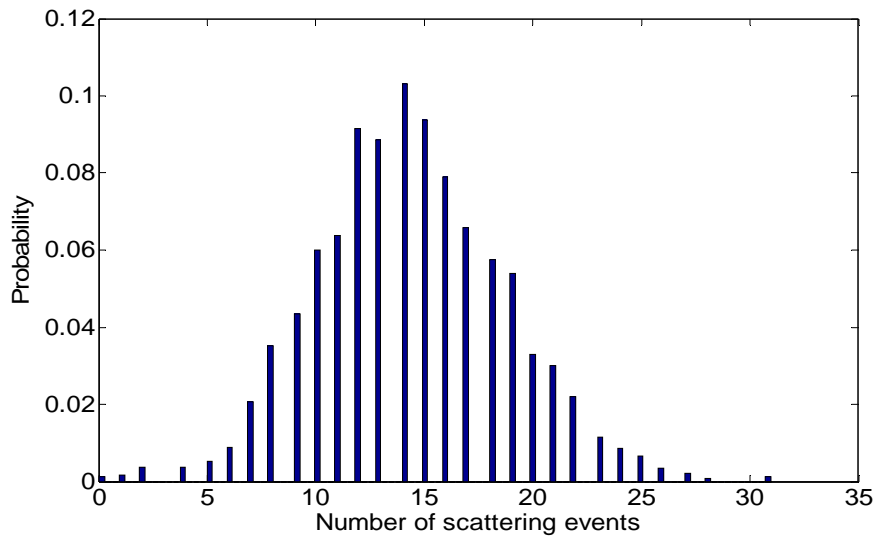


Figure 33. The histogram of the number of scattering events. Only for Cumulus cloud II.

Aperture size (radius): 10cm ; FOV half-angle: 90 degrees; $\tau = 17$.

one scattering. Thus, for the fog oil medium, only the LOS photons (non-scattering) are meaningful to the FOSC system.

However, for cumulus cloud II particles, the situation is completely different. The PDF of the scattering angle for cumulus cloud II has a very strong peak in the forward-scattering direction, and the mean of the scattering angle is around 3 degrees. This implies that for a moderate number of scatterings, light received by the receiver located at the center of the receiver plane is dominated by the photons that have undergone all small angle scattering events [19]. However, even if only one large scattering angle is generated when a photon propagates through clouds, a large value of spatial and angular dispersion may be expected. As a result, a receiver of limited size located at the center of the receiver plane may never catch such a photon. Therefore, for cumulus cloud II, multiple receivers with a large FOV located around the LOS area may help to catch the scattered photon when a large value of optical thickness is concerned in FSOC.

5.7 Conclusions

In this chapter, the relation between energy loss (E_r/E_t) and FOV half-angle is investigated. In the case of fog oil particles, a large FOV half-angle does not help to increase the scattered energy received because of the uniform shape of the phase function and the small value of average scattering distance D_{ave} . However, for cumulus cloud II, a large FOV half-angle helps much to increase the received energy, especially for a large value of optical thickness. It is due to the very strong forward-scattering peak shown in the phase function of cumulus cloud II.

The correlation between spatial and angular dispersion of the received photons is developed. A 2-D histogram of spatial and angular dispersion is drawn to show the correlation.

In the case of fog oil, it is shown that only the LOS photons are meaningful to the FSOC system. However, for cumulus cloud II, a significant number of the scattered photons cluster around the LOS peak. It is also shown that, for cumulus cloud II, when a large value of optical thickness, such as 17, is considered, the FOV half-angle of the receiver does not need to be more than 5 degrees to collect the scattered photons with spatial dispersion less than $2m$. Moreover, the correlation pictures show that the larger spatial dispersion is; the larger angular dispersion will be. This means that if someone tries to collect the photons with large spatial dispersion, a receiver with a large FOV is needed.

The photon density distribution in the $x - y$ receiver plane is investigated. The figures of the photon density distribution only show the photons with spatial dispersion less than $2m$, since the interesting area for the receiver design is the area around the LOS area. For the fog oil, the figures of the photon density distribution show that not many scattered photons exist when spatial dispersion is less than $2m$. Only the LOS peak exists. This means that the scattering effects of fog oil particle are so strong that most spatial dispersion of the received scattered photons is larger than $2m$, which are not shown in these figures.

In the case of cumulus cloud II, when a small value of optical thickness is concerned, a very strong LOS peak is shown in the figures of the photon density distribution. However, when a large value of optical thickness is concerned, photons are mostly uniformly distributed in a circle at least with a radius $2m$. Thus, unlike the case of a small value of optical thickness, the received energy does not fluctuate so much if a receiver is placed inside this circle. Therefore, for cumulus cloud II, multiple receivers located around the LOS area of the receiver plane are proposed to maintain the link availability when a large value of optical thickness is concerned.

Chapter 6

Experimental results for cigarette smoke

6.1 Introduction

Smoke is one type of man-made particles, and the particle density of smoke strongly depends on the method of generating smoke. The particle density of smoke may vary if smoke is generated with different methods or under different situations. As discussed in Chapter 2, the particle density is an important parameter in calculating scattering coefficient $k_s(D_{ave})$. See Equation 2.16, 2.17 and 2.18. All simulation results for fog oil particles (smoke type of particles) are based on particle density $N_0 = 1.07 \times 10^6 \text{ cc}^{-1}$. The fog oil particles are generated by a smoke generator. The particle density is adjustable. If N_0 produced by smoke generators in a battlefield environment is not close to the value used in the simulations, the simulation results should be rescaled. Thus, a method of calculating the particle density of smoke must be found to ensure the accuracy of the simulation results.

This chapter presents an experiment to demonstrate a feasible method of measuring the particle density of smoke. In the experiment, light is transmitted through smoke produced by cigarettes. Cigarette smoke is selected for the experiment for its particular properties, which will be explained later. In Section 2.4, a method was developed to calculate the particle density of smoke. See Equation 2.23. Here, through the equation, the experimental results are used to calculate the particle density of cigarette smoke. The value obtained turns out to be close to other

reported values. The experiment confirms the feasibility of determining the particle density of smoke through Equation 2.23.

The computer simulation results of cigarette smoke are presented in the chapter, as well. The simulation results match the experimental results. It shows that the ray-tracing model is a good physical model simulating light transmitted through smoke.

This chapter is organized as follows. Section 6.2 explains why cigarette smoke is selected for the experiment. Section 6.3 discusses the experimental setup. The experimental procedure and results are presented in Section 6.4. In Section 6.5, the particle density of cigarette smoke is calculated based on the experimental results. In Section 6.6, the computer simulation results of cigarette smoke are presented and compared with the experimental results. Finally, Section 6.7 concludes the chapter with a summary.

6.2 Reasons for selecting cigarette smoke in the experiment

In the experiment, a smoke chamber is used on an optical table in a laboratory. The shape of the smoke chamber is a cylinder. The length of the chamber is 17.78cm , and the radius

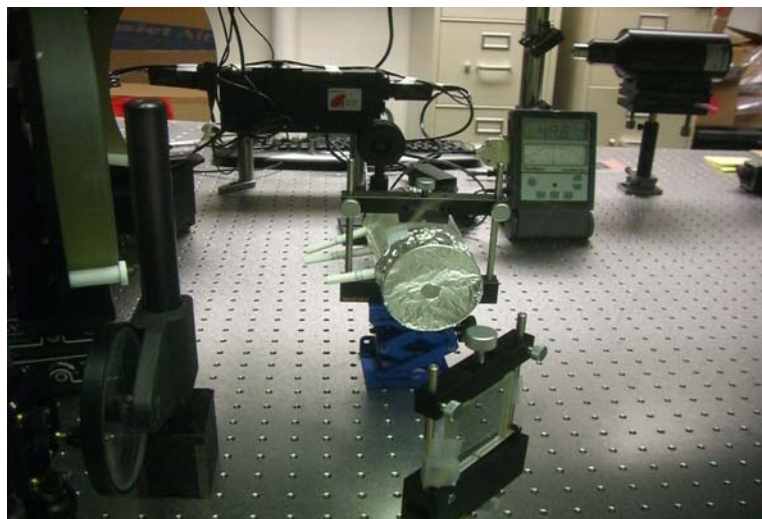


Figure 34. An experiment for light propagating through cigarette smoke.

of it is 3.81cm . Figure 34 shows a smoke chamber on an optical table. There are two reasons that cigarette smoke is selected for the experiment:

- The phase function of cigarette smoke is similar to that of fog oil particles. The reported mean radius of cigarette smoke is $\sim 0.143\mu\text{m}$ at 25°C [27]. The mean radius of fog oil particles is $\sim 0.142\mu\text{m}$. Thus, cigarette smoke can be treated as the fog oil type of scattering medium. As a result, some of the simulation results for fog oil particles shown in Chapter 5 are applicable to cigarette smoke.
- Due to the particle density of fog oil, a smoke chamber built for experiment would require a smoke chamber too large to be built in a lab. The lab environment requires a scattering medium with a very large scattering coefficient, k_s . Cigarette smoke offers a solution. It has a larger particle density than that of fog oil particles. As mentioned in Chapter 2, the larger the particle density is, the larger the scattering coefficient will be. See Equation 2.17. The reported particle density measured in experiments for freshly generated cigarette smoke is $\sim 10^{10}\text{cc}^{-1}$, and coagulation rates ($2\times 10^{-10}\text{cm}^3/\text{s}$ to $5\times 10^{-10}\text{cm}^3/\text{s}$ or less) are slow [28]. The large particle density, and accordingly, the large scattering coefficient of cigarette smoke, allows a manageable size of the smoke chamber to be built in the lab.

Some of the simulation results for fog oil particles shown in Chapter 5 are applicable to cigarette smoke. Here in the experiment, received power is measured by a power meter with a detector diameter 19mm after light is transmitted through the smoke chamber. It assumes that the LOS photons produce the power read by the power meter. The assumption is valid since the shapes of the phase functions of fog oil and cigarette smoke particles are similar. Therefore, the

conclusion on the simulation results of fog oil particles shown in Chapter 5 applies to cigarette smoke, namely, only the LOS photons are meaningful to the detector of the power meter.

Since the length of the smoke chamber is 17.78cm , the effects of non-zero beam divergence of the laser are negligible due to the short length. As a result, Equation 2.23 is simplified as

$$N_0 = \frac{1}{Lch \times k_{\text{normscat}}} \ln\left(\frac{P_t}{P_{\text{LOS}}}\right). \quad (6.1)$$

where $Lch = 17.78\text{cm}$. P_{LOS} is measured by the power meter in the experiment. Normalized scattering coefficient k_{normsca} is not a function of the particle density. According to Mie theory, it can be calculated by the particle size and the refractive index of the particles at a specific wavelength.

6.3 Experimental setup

This section explains how the experiment is set up. The smoke chamber is a plastic bottle with two holes on each end, so the light can go through the chamber without interaction with plastic. Four holes are drilled in the body of the plastic cylinder so that cigarettes can be put into the smoke chamber to generate smoke. Figure 35 shows the scheme of the experimental setup.

6.4 Experimental procedure and results

The wavelength of laser is 810nm . The laser and the power meter are always on axis. The power meter reading is $\sim 623\text{mW}$ without smoke, so the transmitted power from the laser is $\sim 623\text{mW}$.

The procedure of the experiment and results are described as follows:

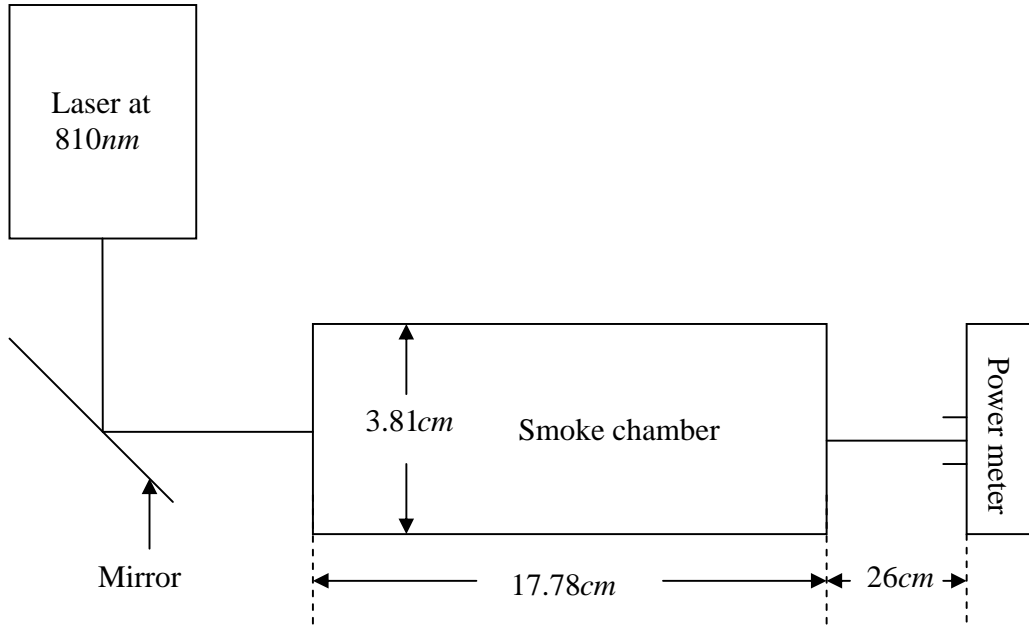


Figure 35. Scheme of the experimental setup.

1. Use one cigarette to generate smoke inside the smoke chamber. After three minutes, the power meter is used to measure the received power for one minute. The reading is unstable, and the received power changes in the range of $[70mW, 100mW]$ within the minute. Large variations of the received power are observed. Thus, when one cigarette is generating smoke, the particle density is a function of time.
2. Use two cigarettes to generate smoke inside the smoke chamber. After three minutes, the power meter is used to measure the received power for one minute. The reading is unstable, and the received power changes in the range of $[60mW, 80mW]$ within the minute. Large variations of the received power are observed. Thus, when two cigarettes are used, the particle density is a function of time.
3. Use three cigarettes to generate smoke inside the smoke chamber. After three minutes, the power meter is used to measure the received power for one minute. The

reading is more stable than the previous two cases. The received power changes in the range of $[40mW, 50mW]$ within the minute. Thus, when three cigarettes are used, smaller variations of the received power are observed.

4. Use four cigarettes to generate smoke inside the smoke chamber. After three minutes, the power meter is used to measure the received power for one minute. The reading is very stable, and the received power changes in the range of $[20mW, 25mW]$ within the minute. Very small variations of the received power are observed. Thus, when four cigarettes are generating smoke, the particle density becomes much more stable.

Table-7 summarizes the experimental results discussed above. It indicates that when four cigarettes are used, the variations of the received power are less than $5mW$ within the minute. It indicates that the particle density is time-invariant in such a situation. In the next section, the particle density of cigarette smoke is calculated based on the experimental results for the four-cigarette case.

Table-7. Experimental results of light transmitted through the smoke chamber.

One minute observation.

Number of cigarettes	Transmitted power (mW)	Reading by power meter (mW)	Power attenuation (dB)
1	623	[70, 100]	[-9.49, -7.94]
2	623	[60, 80]	[-10.16, -8.91]
3	623	[40, 50]	[-11.92, -10.95]
4	623	[20, 25]	[-14.93, -13.96]

6.5 Particle density of cigarette smoke in the four-cigarette case

As mentioned in Section 6.2, the power measured by the power meter is assumed to be the LOS power. As a result, the values shown in the fourth column of Table-7 can be treated as the LOS power, P_{LOS} , when the transmitted power, P_t , is normalized to one watt.

When four cigarettes are used, the particle density of cigarette smoke is stable within one minute observation. Thus, the particle density of cigarette smoke is calculated based on the experimental results of the four-cigarette case (the values shown in the fifth row of Table-7).

Equation 6.1 shows that in order to calculate the particle density, the normalized scattering coefficient, $k_{normsca}$, has to be known first. According to Mie theory, parameter $k_{normsca}$ can be calculated based on the particle size and the refractive index of particles at a specific wavelength. The refractive index of cigarette smoke at wavelength $810nm$ is not available in the literature. The refractive index of cigarette smoke at the visible wavelength is in the range of [1.43, 1.49] with no apparent dependence on the particle size [29]. Thus, the refractive index at the visible wavelength is used here to calculate parameter $k_{normsca}$. The normalized scattering coefficient, $k_{normsca}$, at the visible wavelength for the particle size $0.143\mu m$ is shown in Table-8.

Table-8. Normalized scattering coefficient $k_{normsca}$ at the visible wavelength
for particle size $0.143\mu m$.

Refractive index	1.43 ^a	1.45 ^a	1.47 ^a	1.49 ^a
$k_{normsca}$	1.4615×10^{-5}	1.6×10^{-5}	1.7454×10^{-5}	1.896×10^{-5}

^a: The refractive index of cigarette smoke at wavelength $810nm$ is not available. The refractive index of cigarette smoke at the visible wavelength is used to calculate $k_{normsca}$.

Table-9. Particle density of cigarette smoke. Four cigarettes are used.

Number of cigarettes	$\ln(P_t/P_{Los})$	$N_o(cc^{-1})$
4	~ 3.3	$9.789 \times 10^8 \sim 1.27 \times 10^9$

Table-10. Summarization of the parameters used for the Monte Carlo computer simulation.

Four cigarettes are used

Number of cigarettes	Refractive index ^a	$N_o(cc^{-1})$	$k_s(km^{-1})$	$D_{ave}(m)$	$Lch(m)$
4	1.49	9.789×10^8	18560	0.0539	0.1778

^a: Refractive index of cigarette smoke at the visible wavelength.

According to Equation 6.1, the particle density of cigarette smoke is calculated based on the data shown in Table-8. The results are shown in Table-9. It indicates that the particle density of cigarette smoke is in the order of $10^9 cc^{-1}$, which is much larger than that of fog oil particles.

6.6 Monte Carlo computer simulation results of cigarette smoke

In this section, the Monte Carlo computer simulation results of light transmitted through cigarette smoke are presented. Then, the simulation results are compared with the experimental results of the four-cigarette case shown in Table-7.

Since the refractive index of cigarette smoke at wavelength $810nm$ is not available in the literature, the refractive index of cigarette smoke at the visible wavelength is used and selected as 1.49. The corresponding particle density is $9.789 \times 10^8 cc^{-1}$. As a result, the scattering coefficient, k_s , is $18560 km^{-1}$. The channel length (the length of the smoke chamber), Lch , is selected as $0.1778m$. Table-10 summarizes the parameters used for the Monte Carlo computer simulation for the four-cigarette case. According to Mie theory, the phase function of cigarette smoke at the visible wavelength is calculated, and shown in Figure 36.

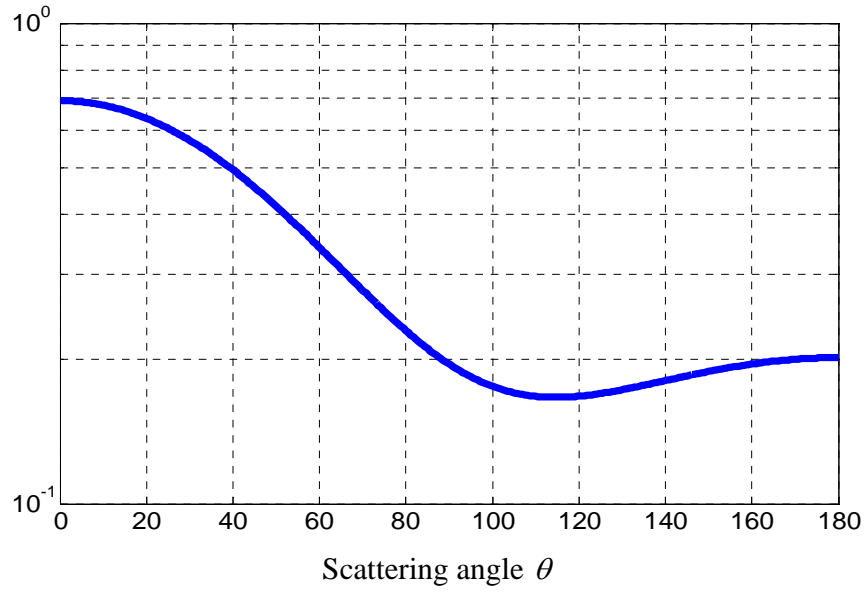


Figure 36. The phase function of cigarette smoke in logarithmic scales at the visible wavelength.

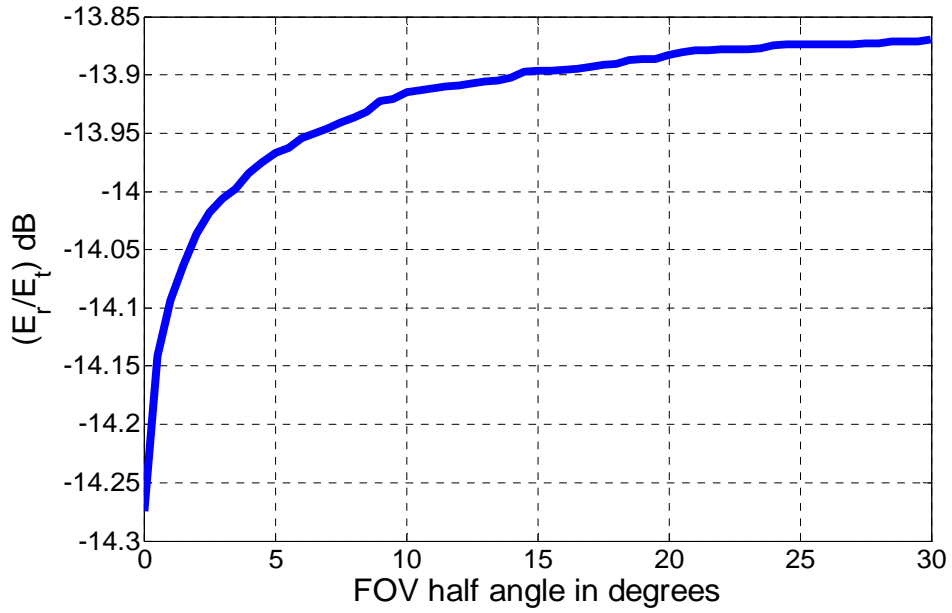


Figure 37. Energy loss versus FOV half-angle for the four-cigarette case.

Optical thickness $\tau = 3.3$ and aperture size is $0.547mm$ in radius.

Figure 37 shows the relation between the FOV half-angle and energy loss for the four-cigarette case. In order to compare with the simulation results for fog oil particles, in the case of cigarette smoke, the aperture size of the receiver in radius is selected as $0.547mm$. The reason is as follows: in the fog oil case, the aperture size of the receiver in radius is selected as $10cm$, which is a regular size used in the FOSC system. However, D_{ave} of fog oil particles ($D_{ave} = 9.86m$) is much larger than that of cigarette smoke ($D_{ave} = 0.0539m$). In order to account the effects of the values of D_{ave} in the computer simulations, the aperture size of the receiver for cigarette smoke has to be rescaled as: $[(0.0539 \times 10)/9.86] = 0.547mm$.

Figure 37 shows that a receiver with a large FOV half-angle does not help to increase the received energy. It shows that only LOS photons are meaningful to the receiver, which is the same conclusion as the fog oil case. In the computer simulation results, the LOS power is $\sim -14.27dB$, which exactly matches the experimental results of the four-cigarette case shown in Table-7.

6.7 Conclusions

In this chapter, the particle density of cigarette smoke is calculated based on the experimental results. The mean radius of cigarette smoke is similar to that of fog oil particles. As a result, the phase function of cigarette smoke is similar to that of fog oil particles. Thus, from the point of view of the phase function, cigarette smoke can be treated as the fog oil type of scattering medium. Equally applicable to both fog oil and cigarette smoke, only the LOS photons are meaningful to the detector of the power meter.

Experimental results of the four-cigarette case are used to calculate the particle density, since it is stable within the time of observation. Here, the particle density of cigarette smoke is in the order of 10^9 cc^{-1} , which is very close to other reported value ($\sim 10^{10} \text{ cc}^{-1}$).

The experiment demonstrates the feasibility of measuring particle density of smoke through the method and Equation 2.23 developed in Chapter 2. Notice that the results here describe only specific scenarios in given situations.

The computer simulation results of cigarette smoke are presented, as well. The simulation results match the experimental results. It shows that the ray-tracing model is a good physical model simulating light transmitted through smoke.

Chapter 7

Conclusions and future work

7.1 Conclusions

This thesis discusses the impact of the physical properties of the scattering medium on the FOSC system design. To narrow the research down to a manageable scope, only energy loss caused by multiple scatterings is analyzed. Signal fading caused by the atmospheric turbulence is not considered.

This research develops a physical model which describes light signal transmitting through the scattering medium. A light pulse consists of numerous photons. Thus, the effects of the scattering medium on transmitted light signals can be treated as a photon-particle interaction. Four parameters govern the photon-particle interaction: absorption probability P_{abs} , scattering angle θ , traveling distance between two consecutive scatterings d , and azimuth angle ϕ . In Mie theory, the PDF of scattering angle θ is called the phase function. Random variable d is an exponential with mean D_{ave} ($1/k_s$). Azimuth angle ϕ is assumed to be a uniform random variable in the range of $[0, 2\pi]$. According to Mie theory, absorption probability P_{abs} , phase functions and parameter D_{ave} are decided by the particle density, the particle size distribution and the refractive index of the medium at a specific wavelength. Generally, multiple scatterings happen before photons reach the medium edge. Scattering events are assumed to be independent of each other. Moreover, in each scattering, the values of the three random variables, θ , d and ϕ ,

are independently generated based on their PDFs. If photons are not absorbed, the scattering paths of photons are solely determined by the generated values.

A Monte Carlo computer simulation model of the physical model is developed. The computer simulations investigate the following issues: 1) the relation among energy loss, FOV, pointing error BC and the aperture size of the receiver; 2) the correlation between spatial and angular dispersion of the received photons distributed in the receiver plane; 3) the photon density distribution in the $x-y$ receiver plane. Finally, the receiver design is proposed based on the simulation results.

Fog oil and cumulus cloud II particles are chosen as the media for the computer simulations, since the scattering effects of the two media are substantially different. The wavelength of FSOC is selected as $1.55\mu m$.

Section 7.2 and 7.3 give summarizes the scattering effects of the two media on the incident light, and receiver design issues based on the simulation results. Section 7.4 offers some suggestions for future work.

7.2 Scattering effects of the fog oil particles and receiver design issues

The phase function of fog oil particles has no peak in the forward-scattering direction at all, and the mean of the scattering angle is around 30 degrees. Thus, in a single scattering event, the scattering effects of the fog oil particles on the incident light are significant. If a photon encounters a fog oil particle, the chance of the photon scattered away with a large scattering angle is high. If multiple scatterings happen, the photon will be scattered far outside the LOS area of the receiver plane. As a result, very large spatial and angular dispersion are expected. Moreover, compared with the other battlefield particles, the average traveling distance between

two consecutive scatterings, D_{ave} , is small. Thus, when channel length Lch is fixed, more scatterings occur when photons travel through the fog oil medium than through most other types of battlefield particles. As a result, the receiver located at the LOS area of the receiver plane may not receive the photons with multiple scatterings. Most photons caught by the receiver located at the LOS area of the receiver plane are the LOS photons (un-scattered photons).

Although a significant number of the scattered photons are received by the receiver plane, most of the scattered photons cannot be caught even by increasing the FOV half-angle of the receiver located at the center of the receiver plane because of the limited size of the aperture size. The computer simulations show that most spatial dispersion of the scattered photons is larger than $2m$. Moreover, the increased number of the scattered photons received by increasing the FOV half-angle is negligible compared to the number of the LOS photons. For the fog oil medium, only the LOS photons are meaningful to the FSOC link budget calculation. Therefore, the fog oil medium requires a sensitive receiver with a small FOV half-angle to find the LOS photons and work with them.

All simulation results for fog oil particles are based on particle density $N_0 = 1.07 \times 10^6 \text{ cc}^{-1}$. The fog oil particles are generated by a smoke generator. The particle density is adjustable. If N_0 produced by smoke generators in a battlefield environment is not close to the value used in the simulations, the simulation results should be rescaled.

7.3 Scattering effects of the cumulus cloud II particles and receiver design issues

The scattering effects of cumulus cloud II particles are different from those of the fog oil particles. The PDF of the scattering angle of cumulus cloud II has a very strong peak in the forward-scattering direction, and the mean of the scattering angle is around 3 degrees. Thus, in a

single scattering event, the scattering effects of cloud particles to the incident photon are negligible compared to the fog oil case. This implies that, for a moderate number of scatterings (at least τ is in the range of $[1, 17]$), light received by the receiver located at the center of the receiver plane is dominated by the photons that have undergone all small angle scattering events. However, even if only one large scattering angle is generated when a photon goes through clouds, a large value of spatial and angular dispersion may be expected. As a result, a receiver of limited size located at the center of the receiver plane may never catch such a photon.

The correlation pictures of spatial and angular dispersion of the received photons show that when a small value of optical thickness is concerned, there is a very strong peak in the LOS area of the dispersion plane. A receiver with a small FOV is proposed to find the LOS photons and work with them. The LOS peak follows an exponential decay. For a large value of optical thickness, the scattered photons play more important roles in the system design. The correlation pictures show that, when a large value of optical thickness is concerned, the FOV half-angle of the receiver does not need to be more than 5 degrees to collect the scattered photons if spatial dispersion is less than $2m$ (pointing error $BC \leq 2m$). Therefore, if a large value of optical thickness is concerned in FSOC, a receiver with a large FOV (less than 5 degrees) is needed to collect the scattered photons.

Multiple receivers are proposed to increase the received energy when a large value of optical thickness is concerned. The photon density distribution in the $x-y$ receiver plane shows that the photons with spatial dispersion less than $2m$ are almost uniformly distributed in the receiver plane when optical thickness $\tau=17$. Unlike the case of a small value of optical thickness, there are no preferred areas where a receiver should be located. Therefore, when a

large value of optical thickness is concerned, multiple receivers may be placed at the receiver plane around the LOS area to maintain the link availability.

7.4 Future work

As mentioned in Chapter 1, scattering loss L_s consists of two parts: one is energy loss (E_r/E_t) , and the other, $[1 + (\Delta t/T_r)]$, is loss due to pulse spread. In this thesis, only energy loss is considered. However, pulse spread Δt plays an important role in the FSOC system design, as well. As shown in Equation 1.3, large pulse spread may increase scattering loss. Similar to energy loss, pulse spread is a function of medium length, medium type, physical size of the receiver (aperture size and FOV) and pointing error, as well.

Generally, when a receiver with a large FOV is used, received energy E_r increases since more scattered photons are collected. However, pulse spread Δt may also increase, which limits the data rate. The bandwidth of the optical channel depends on pulse spread. Thus, the combination effects of energy loss and pulse spread have to be considered in the FSOC system design. Experimental results have showed that when optical thickness is less than 18, observed pulse spread is never more than $20ns$ with some specific sizes of the receiver used.

The above observation suggests that future studies could be devoted to determine the relation among pulse spread, energy loss and scattering loss, and to find a receiver structure which will maximize the received power and minimize pulse spread.

Bibliography

1. Juan C. Juarez, Anurag Dwivedi, A. Roger Hammons, Jr. Steven D. Jones, Vijitha Weerackody, and Robert A. Nichols, "Free-space optical communications for next-generation military networks," IEEE Communications Magazine, pp. 46-51, November, 2006.
2. Xiaoming Zhu and Joseph M. Kahn, "Free-space optical communication through atmospheric turbulence channels," IEEE Transactions on Communications, pp. 1293-1300, Vol. 50, NO.8, August, 2002.
3. G. C. Mooradian, M. Geller, L. B. Stotts, D. H. Stephens and R. A. Krautwald, "Blue-green pulsed propagation through fog," Applied Optics 18, pp. 429-441, 1979.
4. John C. Matter and Robert G. Bradley, "Optical pulse propagation through clouds," Applied Optics 20, pp. 2220-2228, 1981.
5. "Smoke screen," Wikipedia, The free Encyclopedia. [Online]. Available at:
http://en.wikioedia.org/wiki/smoke_screen.
6. Scoot Stout, "Battle assesses risks of fog oil smoke." [Online]. Available at:
<http://www.battelle.org/Enviroment/publications/envUpdates/Special2000/article4.html>.

7. G. C. Mooradian and M. Geller, "Temporal and angular spreading of blue-green pulses in clouds," *Applied Optics* 21, pp. 1572-1577, 1982.
8. E. A. Bucher, "Computer simulation of light pulse propagation for communication through thick clouds," *Applied Optics* 12, pp. 2391-2400, 1973.
9. A. P. Ciervo, "Propagation through optically thick media," *Applied Optics* 34, pp. 7137-7148, 1995.
10. S. Arnon, D. Sadot and N. S. Kopeika, "Simple mathematical models for temporal, spatial, angular and attenuation characteristics of light propagating through the atmosphere for space optical communication: Monte Carlo simulations," *Journal of Modern Optics* 41, pp. 1955-1972, 1994.
11. S. Arnon, D. Sadot, and N. S. Kopeika, "Analysis of optical pulse distortion through clouds for satellite to earth adaptive optical communication," *Journal of Modern Optics* 41, pp. 1591-1605, 1994.
12. S. Arnon and N. S. Kopeika, "Adaptive optical transmitter and receiver for space communication through thin clouds," *Applied Optics* 36, pp. 1987-1993, 1997.
13. A. S. Jursa, *Handbook of geophysics and the space environment*, Air Force Geophysics Laboratory, United States Air Force, 1985.

14. Djafar K. Mynbaev and Lowell L. Scheiner, *Fiber-Optic Communications Technology*, Prentice Hall, 2001.
15. Ajoy Ghatak and K. Thyagarajan, *Introduction to fiber optics*, Cambridge University Press, 1998.
16. Richard C. Shirkey and David H. Tofsted, "Electro-Optical Aerosol Phase Function Database, PFNDAT2005," Army research Laboratory, 2005.
17. F. Smith, *The Infrared & Electro-optical Systems Handbook: Atmospheric Propagating of Radiation*, Vol.2, SPIE PRESS, 1993.
18. Belal Y. Hamzeh, "Multi-rate Wireless Optical Communications in Cloud Obscured Channels," Ph.D. Thesis, The Pennsylvania State University, 2005.
19. V. De. Hulst, *Light Scattering by Small Particles*, Wiley, New York, 1957.
20. David H. Pollock, *The Infrared & Electro-optical Systems Handbook: Countermeasure Systems*, Vol.7, SPIE PRESS, 1993.
21. W. M. Farmer, R. D. Morris, and F. A. Schwartz, "Optical particle size measurements of hygroscopic smokes in laboratory and field environments," *Applied Optics* 20, pp. 3929-3940, 1981.

22. Weast R. C. and Astle M. J., *Handbook of Chemistry and Physics*, 61st Edition, CRC Press: Boca Raton, 1980-1981.
23. Ivlev L.S and Popova S.I, "The complex refractive indices of substances in the atmosphere aerosol dispersed phase," *Atmospheric and Oceanic Physics*, pp. 359, 1973.
24. Gillespie J.B and Lindberg J.D, "Seasonal and geographic variations in imaginary refractive index of atmospheric particulate matter," *Applied Optics* 31, pp. 2107-2111, 1992.
25. D. Deirmendjian, "Scattering and polarization properties of water clouds and hazes in the visible and infrared," *Applied Optics* 3, pp. 187-196, 1964.
26. S. Karp, R. M. Gagliardi, S. E. Moran, and L. B. Stotts, *Optical Channel: Fibers, Clouds, Water and the Atmosphere*, Springer, 1988.
27. Ravindra Pratap singh, Virendra kumar Jaiswal and Vinod Kumar Jain, "Study of smoke aerosols under a controlled environment by using dynamic light scattering," *Applied Optics* 45, pp. 2217-2221, 2006.
28. Ramkuber Yadav, Khaled Saoud, Firooz Rasouli, Mohammad Hajaligol and Robert Fenner, "Study of cigarette smoke aerosol using time of flight mass spectrometry," *Journal of Analytical and Applied Pyrolysis* 72, pp. 17-25, 2004.

29. D. D. McRae, "The refractive index of individual cigarette smoke droplets," *J. Colloid Interface Sci.* 87, 117–123, 1982.

Vita

Binbin Wu

Binbin Wu was born in 1978, in Beijing, China. He received his B.E. degree in Communications Engineering from Yunnan University, Kunming, China in 2001, following which he joined Beijing Mobile, Beijing, China as an engineer. In 2002, he started his graduate study in Electrical Engineering at the University of Alabama in Huntsville, Huntsville, USA. He obtained the M.S. degree in 2004. Afterwards, he continued onto Ph.D. work in Electrical Engineering at the Pennsylvania State University in 2005. He joined the Center for Information and Communications Technology Research (CICTR) at the Pennsylvania State University in 2005, where he worked as a graduate research assistant. He is expected to obtain the Ph.D. degree in December, 2007.

His research interests include broadband communications, optical communications and digital signal processing.